AERODYNAMIC CHARACTERISTICS OF AN AXISYMMETRIC BODY UNDERGOING A UNIFORM PITCHING MOTION

Lloyd Henry Smith

UNCLASSIFIED

SECURITY CLASSIFICATION OF THIS PAGE (When Data Entered)

REPORT DOCUMENTATION PAGE

READ INSTRUCTIONS BEFORE COMPLETING FORM

1. REPORT NUMBER

2. GOVT ACCESSION NO.

3. RECIPIENT'S CATALOG NUMBER

4. TITLE (and Subtitle)
AERODPNAMIC CHARACTERISTICS OF AN AXISYMMETRIC BODY UNDERGOING A UNIFORM PITCHING MOTION

5. TYPE OF REPORT & PERIOD COVERED
Doctor's Dissertation
December 1974

6. PERFORMING ORG. REPORT NUMBER

7. AUTHOR(s)
Lloyd H. Smith
Naval Weapons Center
China Lake, California 93555

8. CONTRACT OR GRANT NUMBER(s)

9. PERFORMING ORGANIZATION NAME AND ADDRESS
Naval Postgraduate School
Monterey, California 93940

10. PROGRAM ELEMENT, PROJECT, TASK AREA & WORK UNIT NUMBERS

11. CONTROLLING OFFICE NAME AND ADDRESS
Naval Postgraduate School
Mechanical Engineering Department

12. REPORT DATE
December 1974

13. NUMBER OF PAGES
100

14. MONITORING AGENCY NAME & ADDRESS(if different from Controlling Office)
Naval Weapons Center
Systems Development Department (Code 51)
China Lake, California 93555

15. SECURITY CLASS. (of this report)
Unclassified

15a. DECLASSIFICATION/DOWNGRADING SCHEDULE

16. DISTRIBUTION STATEMENT (of this Report)
Approved for public release; distribution unlimited

17. DISTRIBUTION STATEMENT (of the abstract entered in Block 20, if different from Report)

18. SUPPLEMENTARY NOTES

19. KEY WORDS (Continue on reverse side if necessary and identify by block number)
Axisymmetric body
Aerodynamics
Pitching motion
High angle of attack

20. ABSTRACT (Continue on reverse side if necessary and identify by block number)
An experimental investigation was conducted to determine the effect of a uniform pitching motion on a slender axisymmetric body while undergoing large excursions in angle of attack. Force and moment measurements were obtained for a slender tangent-ogive/cylindrical body over a range of Reynolds numbers from $5X10^4$ to $1.4X10^5$ while varying the angle of attack from zero to 90 degrees and the pitch rate between zero and 281 degrees per second. Smoke flow visualization studies were used as an aid in assessing wake vortex transitions.

DD FORM 1 JAN 73 1473 EDITION OF 1 NOV 65 IS OBSOLETE
S/N 0102-014-6601

Aerodynamic Characteristics of an Axisymmetric Body Undergoing a Uniform Pitching Motion

by

Lloyd Henry Smith
Naval Weapons Center Fellow

Submitted in partial fulfillment of the
requirements for the degree of

DOCTOR OF PHILOSOPHY

from the
NAVAL POSTGRADUATE SCHOOL
December 1974

ABSTRACT

An experimental investigation was conducted to determine the effect of a uniform pitching motion on a slender axisymmetric body while undergoing large excursions in angle of attack. Force and moment measurements were obtained for a slender tangent-ogive/cylindrical body over a range of Reynolds numbers from $5X10^4$ to $1.4X10^5$ while varying the angle of attack from zero to 90 degrees and the pitch rate between zero and 281 degrees per second. Smoke flow visualization studies were used as an aid in assessing wake vortex transitions.

The results of the investigation show that there is an increment of normal force directly attributable to the uniform pitching motion. The incremental increase in the normal force is sufficient to cause significant errors in calculating body damping derivatives from static force measurements. Distinct wake vortex transitions at approximately 20, 50 and 65 degrees were observed. The effect of a uniform pitching motion shifts the angle of attack at which these wake vortex transitions occur, and can reduce the abruptness of those transitions.

TABLE OF CONTENTS

LIST OF TABLES

LIST OF FIGURES

LIST OF SYMBOLS

A	reference area, $\pi d^2/4$
b	radius of circular cross-section of body
C_D	two dimensional drag coefficient
C_m	pitching moment coefficient, $\frac{\text{pitching moment}}{\frac{1}{2}\rho V_o^2 Ad}$
C_N	normal force coefficient, $\frac{\text{normal force}}{\frac{1}{2}\rho V_o^2 A}$
C_n	yaw moment coefficient, $\frac{\text{yaw moment}}{\frac{1}{2}\rho V_o^2 Ad}$
C_Y	yaw force coefficient, $\frac{\text{yaw force}}{\frac{1}{2}\rho V_o^2 A}$
d	diameter of circular cross-section of body
g	spacing between shed vortices, [Ref. 18]
ℓ	effective length of circular cross-section of a finite length body
R_e	freestream Reynolds number, $\frac{dV_o}{\nu}$
R_{e_c}	crossflow Reynolds number, $\frac{dV_o \sin\alpha}{\nu}$
S	Strouhal number, $\frac{fd}{V_o \sin\alpha}$
V_o	freestream velocity
X	potential force perpendicular to velocity
Y	potential force parallel to velocity
α	angle of attack
$\dot{\alpha}$	time rate of change of angle of attack, pitch rate

Γ	vortex strength (positive counterclockwise)
ζ	complex coordinate
η	ratio of the drag coefficients for a finite and an infinite length circular cylinder
Ω	complex velocity potential, $(d\Omega/d\zeta = u - iv)$

ACKNOWLEDGEMENTS

The author is truly indebted to Professor R. H. Nunn for his inspiration, guidance, and continued support during this research project and throughout the course of studies. Professor T. Sarpkaya is gratefully acknowledged for his contribution of the research topic and his willing efforts in preparing the author for this research.

The strain gage balance used during the experiments was on loan from the Naval Ship Research and Development Center, Carderock, Maryland. Their generosity resulted in a significant time and cost saving in conducting the experiments.

Finally, the author wishes to acknowledge the support of the Naval Weapons Center, China Lake, California, who provided the fellowship for advanced academic training at the Naval Postgraduate School, and whose sponsorship made this research possible.

INTRODUCTION

Certain evolving tactical missile missions require extreme flight agility to accomplish large and rapid heading changes. Such requirements have prompted an interest in the aerodynamic loading of slender missile configurations at large angles of attack and while undergoing rapid pitching through large excursions in angle of attack. A considerable amount of recent research has been directed toward understanding the static aerodynamics of slender bodies of revolution at moderate and high angles of attack. These efforts have revealed that the flow on the leeside of these bodies is characterized by a vortex system that changes with increasing angle of attack from a steady symmetric pair of rolled-up vortex sheets to steady asymmetric shedding of discrete vortices and, finally, at large angles of attack, to an unsteady asymmetric arrangement. Associated with these changing wake vortex patterns are significant yawing forces and moments, which can be larger than the control moments produced by the deflection of conventional control devices. These body generated forces and moments or the interference of the trailing vortices with wings and tails can have a dominant effect on the manuevering characteristics of a missile.

The emphasis of the present experimental investigation has been placed upon a study to (1) determine the dependence of the aerodynamic loading upon a uniform angular velocity in pitch, and (2) identify specific transition regions in the wake vortex pattern and the subsequent alteration of those patterns due to the rotation. It is realized that for full scale vehicles in flight there exists the possibility of coupling between the shedding of the wake vortices and

the translational motion of the missile. Hence, the results of a wind tunnel investigation using a model, the movement of which is restrained by its mounting system, may not be directly applicable to full scale vehicles. However, the effects on the wake vortex configuration of certain variables such as pitch rate and Reynolds number may indicate significant trends.

The experimental phase of this study was carried out in a low turbulence subsonic wind tunnel facility especially designed and instrumented for this purpose. The aerodynamic forces and moments acting upon a tangent-ogive/cylindrical body, rotating at a constant angular velocity about an axis normal to the axis of symmetry in an otherwise uniform flow, were recorded for Reynolds numbers of $5X10^4$, $8X10^4$ and $1.4X10^5$ based on a maximum body diameter. The angle of attack was varied between zero and 90 degrees, and the rate of pitch was varied between zero and approximately 300 degrees per second. The surrounding flow field was visually displayed by means of a multiple filament smoke technique.

In subsequent sections of this dissertation some background material and the nature of the problem are developed, the experimental equipment and procedures are described, and the results are presented together with their implications regarding flow phenomena at high incidence and the design of highly maneuverable missiles.

NATURE OF THE PROBLEM

As a body of revolution is exposed to an increasing angle of attack, the flow on its leeward side separates and rolls up to form vortices. Under these conditions, normal force and pitching moment can no longer be predicted by slender body theory. For angles of attack less than approximately 20 degrees (depending on the crossflow Reynolds number) two symmetric vortices form as illustrated in Figure 1. For larger angles of attack discrete vortices grow asymmetrically and break away or are shed from the leeward side, at first in a spatially periodic manner as shown in Figure 2, while at the higher angles the shedding becomes unsteady.

Analyses of the flow about inclined bodies of revolution have been presented by numerous investigators, incorporating varying degrees of rigor. Almost exclusively these analyses have used the impulsive flow analogy proposed by Allen and Perkins [Ref. 1]. This analogy assumes that the crossflow is swept down the length of the body at a rate $V_o \cos\alpha$. At each axial station the flow field is taken to be analogous to the flow about a cylinder in crossflow, whose radius is equal to the body radius at that axial station. The developing (with axial position) crossflow is thus similar to the flow about a cylinder impulsively set in motion from rest. The validity of the impulsive flow analogy depends upon crossflow independence; that is, the viscous flow across the cylinder may be treated independently of the flow along the cylinder. This is only strictly true for laminar boundary layers.

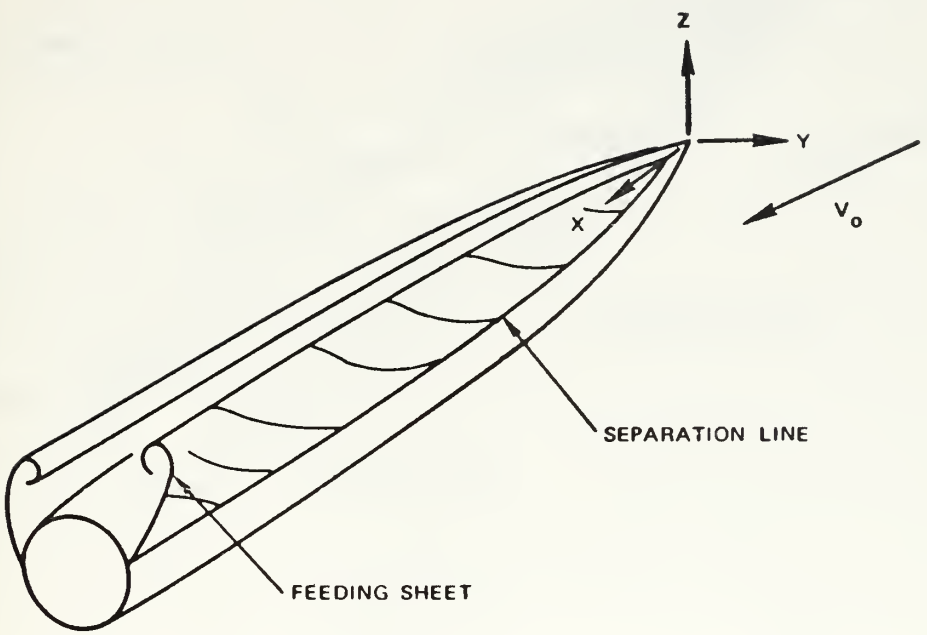

Figure 1. Symmetric vortex arrangement on an inclined body of revolution

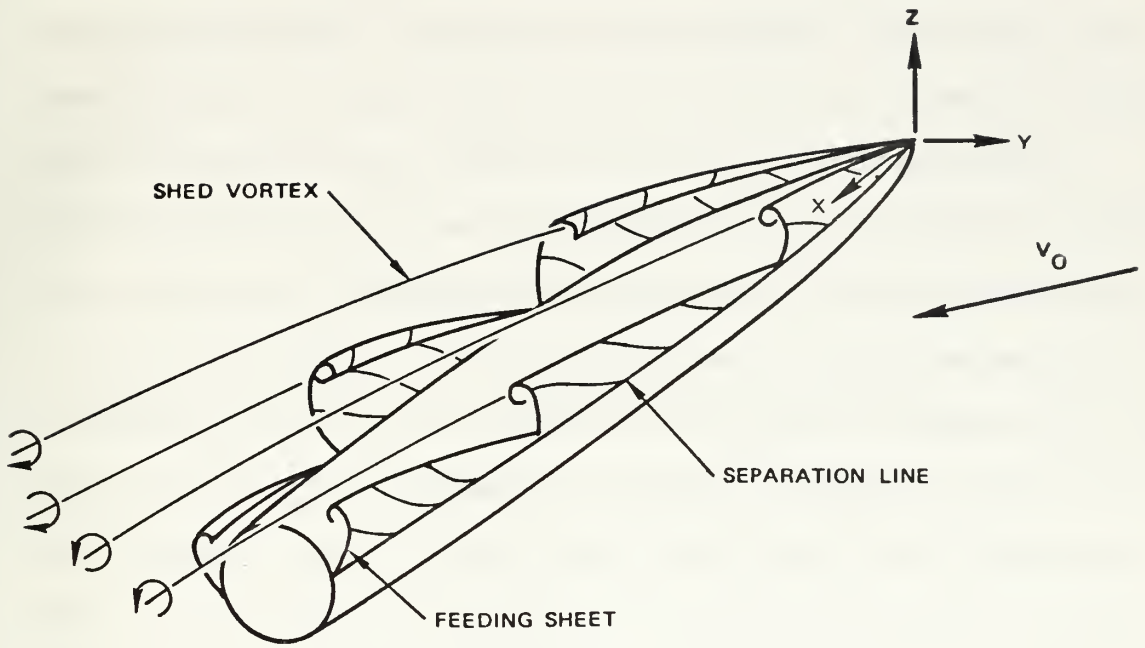

Figure 2. Asymmetric vortex shedding on an inclined body of revolution

The crossflow Reynolds number at any particular axial station depends upon the angle of attack and the body diameter at that station. Thus, at a specific angle of attack the flow as viewed in crossflow planes develops with increasing crossflow Reynolds number along the nose section, reaching a constant maximum value at the junction of the nose and the afterbody. Near the apex of the nose the crossflow Reynolds number is very low (small body diameter), so that the viscous action is large in comparison to the inertia of the fluid and separation does not occur. As the crossflow Reynolds number increases with increasing axial position, a symmetric vortex pair is formed. At still higher crossflow Reynolds numbers alternate detachment of the vortices on the leeward side of the body takes place, and so on. For a given angle of attack and freestream Reynolds number the crossflow Reynolds number achieves its maximum value along the afterbody. It is this maximum value of the crossflow Reynolds number that determines the final stage of vortex development along the body.

An historical sketch of the evolution of the qualitative models and the methods of analysis for angles of attack up to about 40 degrees is presented in Ref. 2. The methods range from engineering calculations for determining normal forces and pitching moments [Refs. 3 to 6], to detailed flow field descriptions which provide information on the separation of the boundary layer fluid and the growth and detachment of the vortices [Refs. 7 to 11]. The prediction of yaw forces, which arise from the asymmetries in the vortex wake, is only achieved using the more complete detailed flow field descriptions. The technique most commonly used in formulating the more complete flow field descriptions is the impulsive flow analogy. Use of the analogy reduces the

three dimensional problem to a two dimensional axially varying (time and axial position are related by $t = x/V_o \cos\alpha$) analysis. Further, the viscous and the potential flow contributions are treated independently and then superimposed.

Concentrating on a potential flow description of the vortex wake, the static forces developed for either the symmetric or spatially periodic asymmetric vortex configurations can be calculated provided the strengths and positions of the wake vortices can be described. The strengths and positions of the vortices are determined by requiring the force on each vortex to balance the force on its feeding sheet, and by specifying that the separation points be stagnation points of the crossflow. Reference 11 is one of the latest examples of this approach which was introduced by Bryson [Ref. 7].

In order to estimate what the effect of a uniform pitching motion might be on an inclined body of revolution consider the components of the velocity in the crossflow planes. As shown in Figure 3, the crossflow velocity is composed of two components, (1) the normal velocity due to the angle of attack and (2) the normal velocity due to the angular velocity. When these two components of crossflow velocity are added they yield a nonuniform velocity distribution along the length of the body. Since the angle of attack is a function of time, $\alpha = \dot{\alpha}t$, the nonuniform velocity distribution along the body is unsteady. Therefore, even though the freestream is steady, and the angular velocity is constant, the crossflow is unsteady.

The effects of an unsteady crossflow can be illustrated by considering a stationary circular cylinder immersed in a time dependent

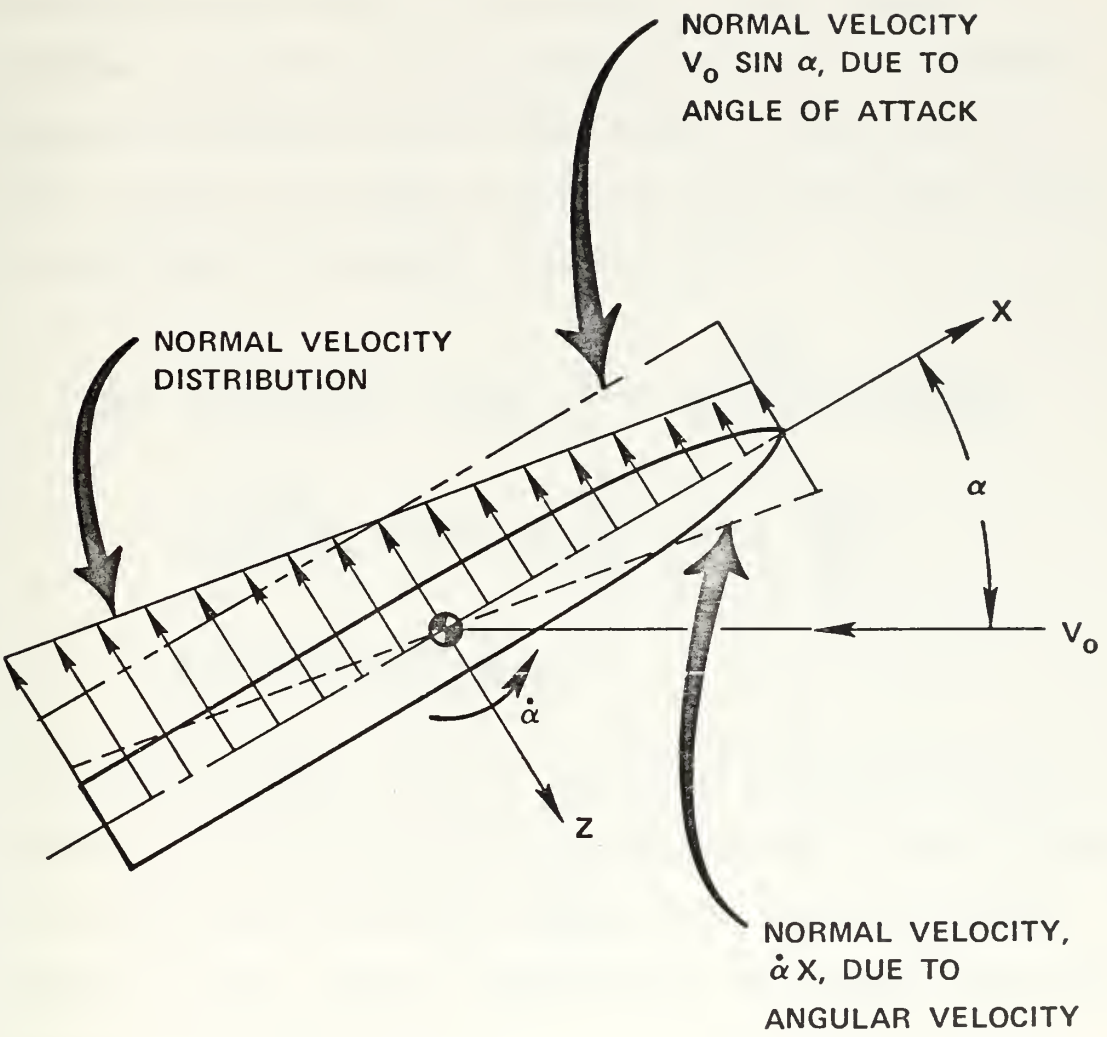

Figure 3. Velocity distribution on an inclined body of revolution while undergoing a uniform pitching motion

flow in the presence of "n" discrete vortices. Using the methods of potential flow theory and the notation shown in Figure 4, the complex potential for the circle in the presence of a time dependent, but otherwise uniform flow, and "n" discrete vortices can be developed through the application of the Circle theorem. A source term is added to displace the stream by an amount equal to the local slope of the body contour. The complex potential is then

$$\Omega = -i\,(V_o \sin\alpha - \dot{\alpha}x)(\zeta - \frac{b^2}{\zeta}) - \frac{i}{2\pi}\sum_{k=1}^{n}\Gamma_k \ln(\zeta - \zeta_k)$$

$$-\frac{i}{2\pi}\sum_{k=1}^{n}\Gamma_k \ln(\zeta) + \frac{i}{2\pi}\sum_{k=1}^{n}\Gamma_k \ln(\zeta - \frac{b^2}{\bar{\zeta}_k})$$

$$+ b\,V_o \cos\alpha \frac{db}{dx}\ln(\zeta)$$

The terms on the right represent respectively the uniform flow and a doublet at the origin, the "n" real vortices, the "n" image vortices at the origin and at the points $b^2/\bar{\zeta}_k$, and the source required to displace the flow. Figure 5 illustrates the relationship between the variables in the source term.

The forces acting on the circle are obtained by applying the Blasius theorem, that is

$$X - iY = \frac{i\rho}{2}\int_c \left(\frac{d\Omega}{d\zeta}\right)^2 d\zeta + i\rho\frac{\partial}{\partial t}\int_c \bar{\Omega}\, d\bar{\zeta}$$

where X and Y represent the yaw and normal forces respectively on the circular body. The total force acting on the circle will be separated into

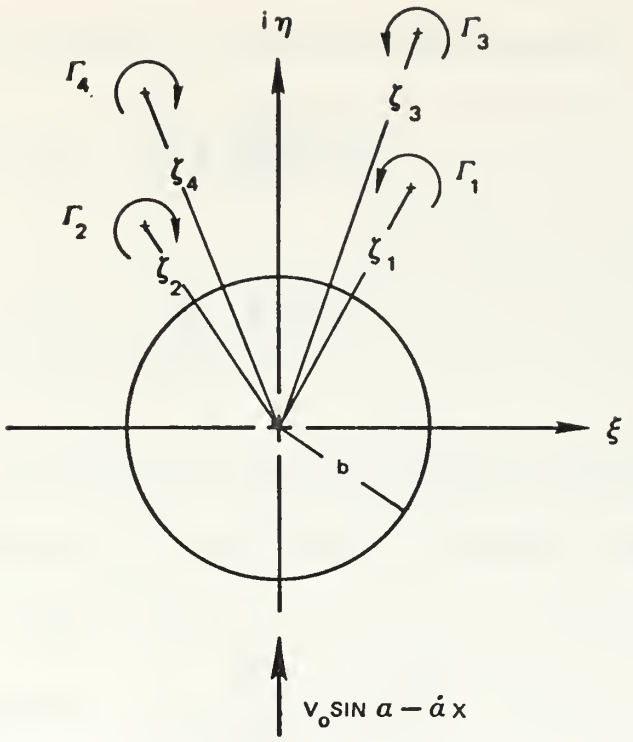

Figure 4. Notation for potential flow analysis

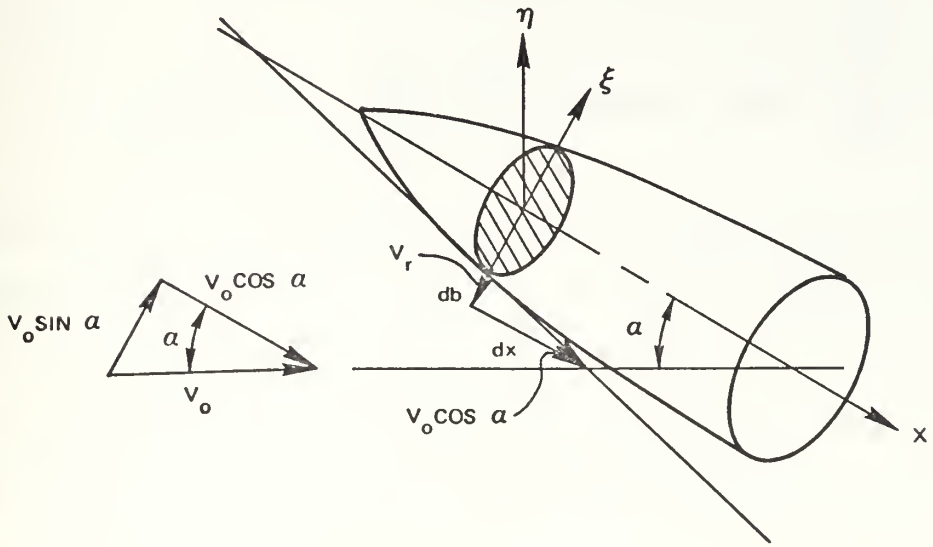

Figure 5. Relationship of variables involved in source term

contributions due to steady and unsteady motions, where

$$X_s - iY_s = \frac{i\rho}{2}\int_c \left(\frac{d\Omega}{d\zeta}\right)^2 d\zeta$$

and

$$X_u - iY_u = i\rho\frac{\partial}{\partial t}\int_c \bar{\Omega}\, d\bar{\zeta}$$

The steady force contribution can be evaluated by either performing the contour integration or by using Lagally's theorem. The first method was used to obtain the result

$$X_s - iY_s = -\rho(V_o \sin\alpha - \dot{\alpha}x)\sum_{k=1}^{n}\Gamma_k\left(\frac{b}{\zeta_k}\right)^2$$

$$+\frac{\rho}{2\pi}\sum_{k=1}^{n}\sum_{j=1}^{n}\Gamma_k\Gamma_j\left[\frac{b^2}{\zeta_k(\zeta_k\bar{\zeta}_j - b^2)}\right]$$

$$+ i\rho b V_o \cos\alpha\frac{db}{dx}\left[2\pi(V_o\sin\alpha - \dot{\alpha}x) - \sum_{k=1}^{n}\Gamma_k\left(\frac{1}{\zeta_k}\right)\right]$$

In general all of the terms on the right will have both real and imaginary parts, thus, both a normal force and a yaw force will be present. Inspection of the steady force equation easily reveals an increment of steady body force due to the angular velocity. The first term containing the pitch rate yields an increment of body force whose direction is dependent upon the vortex configuration. For example, for a symmetric vortex pair only imaginary terms remain in the force equation, and the effect of pitch rate is to decrease the normal force for positive values of x (where x is measured from the axis of

rotation, positive toward the apex of the nose), and to increase the normal force for negative values of x. Thus, the choice of the axial station about which the body is rotated will directly influence the magnitude of the body force for uniform pitching.

The unsteady force contribution is obtained by first taking the complex conjugate of the unsteady force equation, that is

$$X_u + i Y_u = - i \rho \frac{\partial}{\partial t} \int_c \Omega \, d\zeta$$

and then integrating by parts, noting that $\Omega\zeta|_c$ vanishes provided no singularities lie on the contour.[1] Then, the unsteady force equation

$$X_u + i Y_u = i \rho \frac{\partial}{\partial t} \int_c \zeta \left(\frac{d\Omega}{d\zeta}\right) d\zeta$$

can be evaluated. The result obtained by performing the indicated contour integration is

$$X_u + i Y_u = \frac{\partial}{\partial t} \left[2\pi i \rho b^2 (V_0 \sin\alpha - \dot{\alpha} x) - i \rho \sum_{k=1}^{n} \Gamma_k \left(\frac{b^2}{\bar{\zeta}_k}\right) \right]$$

Completing the process by taking the partial derivatives with respect to time, obtain

$$X_u + i Y_u = 2\pi i \rho b^2 V_0 \cos\alpha \, \dot{\alpha} - i \rho \sum_{k=1}^{n} \Gamma_k \frac{\partial}{\partial t} \left(\frac{b^2}{\bar{\zeta}_k}\right) - i \rho \sum_{k=1}^{n} \left(\frac{b^2}{\bar{\zeta}_k}\right) \frac{\partial \Gamma_k}{\partial t}$$

---

[1] Private communication with Prof. T. Sarpkaya, Naval Postgraduate School, Monterey, California, 1972.

Therefore, had the crossflow not been time dependent the first term on the right would not be present, and the unsteady forces would only be a result of the vortex configuration. The presence of the first term shows that the pitch rate does contribute an increment of normal force (the term is always imaginary). The effect of this term is to increase the normal force, regardless of where the axis of rotation is located.

Although the presence of an increment of body force due to the angular motion has been illustrated, the magnitude and direction of the increment for an instantaneous angle of attack can only be resolved via a complete analysis of the vortex wake configuration. This analysis did, however, indicate that the steady body force is not only dependent upon the angular velocity but also upon the location of the axis of rotation. If the axis of rotation were placed at the apex of the body (x always negative), the effect of the angular motion would be to increase the normal force with increasing angular velocity. This result was demonstrated in an investigation conducted by Sarpkaya [Ref. 12] for a rotating flat plate in a uniform flow. Glauert [Ref. 13], obtained a similar result in an analysis of the lift and pitching moment on an airfoil due to a uniform angular velocity of pitch. These results also indicate that it is possible to rotate the body about an axis such that the increment of body force due to a constant angular velocity could be nullified.

EXPERIMENTAL APPARATUS AND PROCEDURES

Most of the experimental apparatus was designed and constructed explicitly for this investigation. The apparatus centered about the Mechanical Engineering Department's subsonic low turbulence wind tunnel, in which the pitch rate mechanism and the multiple filament smoke system were installed.

The primary independent variables included in the study were (1) the freestream Reynolds number, (2) angle of attack and (3) pitch rate. This selection of independent variables was not meant to imply that they are the only variables, or even the most important. For instance, nose shape, body fineness, freestream turbulence and compressibility are all other independent variables which could influence the aerodynamic loads. However, all known independent variables not under investigation were purposefully held constant. Normal force and pitching moment were selected as the primary dependent variables, while yaw force and yaw moment were given secondary consideration even though the existence of yaw loads at high angles of attack has been illustrated by numerous investigators. Axial force and rolling moment were not evaluated since they are practically nonexistent for a slender axisymmetric body.

The extent to which measured aerodynamic loads fully describe the causes of particular phenomena is questionable due to their integrated character. Therefore, as a supplement to the main objective of this research, a flow visualization study of the wake region was conducted. This effort is described in Appendix A.

LOW TURBULENCE SUBSONIC WIND TUNNEL

Figure 6 is a photograph of the wind tunnel test section and the instrumentation assembled for this investigation. The tunnel is of open circuit design with its intake inside the building and exhausting outside. The test section is 20 inches by 28 inches at the center and is eight feet long. The prime mover is a six blade axial fan, located at the downstream end, and driven by a variable speed 75 horsepower electric motor. The wind speed is continuously variable from 30 to 300 feet per second when the test section is clean, and from about 50 to 250 feet per second when the model and pitch rate apparatus are installed. The freestream turbulence intensity is controlled by means of a six inch thick honeycomb flow straightener located at the plenum entrance, followed by up to five graded screens (interchangeable) and an area contraction of ten to one.

Prior to experimentation with the model a complete survey of the test section flow quality was accomplished. Surveys were made in each of the three coordinate directions using a hot wire anemometer and an EAI 1300 variplotter. Vertical velocity profiles were recorded at various lateral and longitudinal stations, lateral profiles at various vertical and longitudinal stations, and longitudinal profiles at various vertical and lateral stations. Figure 7 is a typical vertical velocity profile between the boundary layers at a nominal freestream velocity of 150 feet per second. The recorded anemometer output voltage, E, is related to the freestream velocity, V, by

$$V = \left(\frac{E^2 - E_o^2}{\beta}\right)^2$$

where E_o is the zero velocity anemometer output voltage and β is a

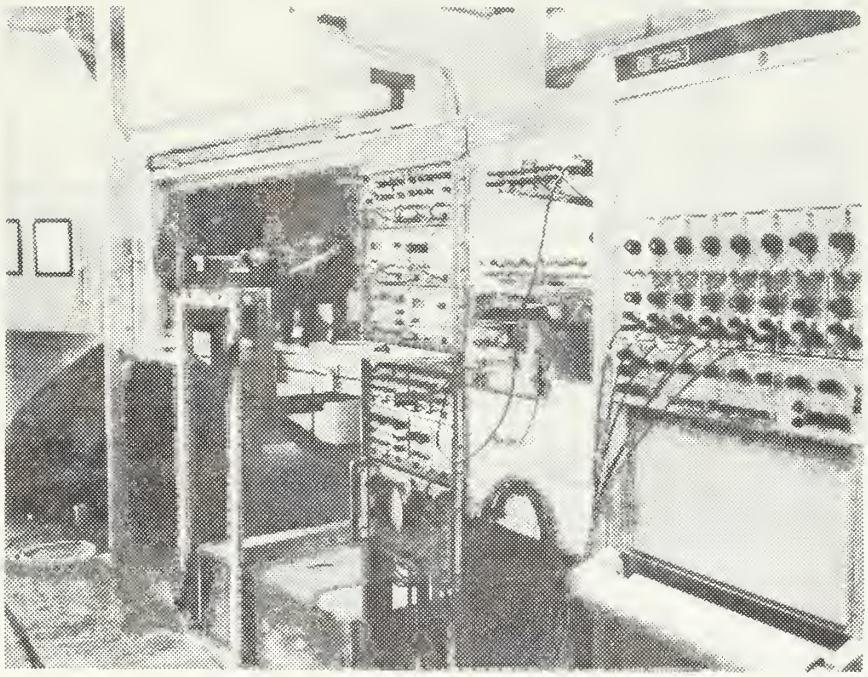

Figure 6. Wind tunnel test section as viewed from instrumentation and control side

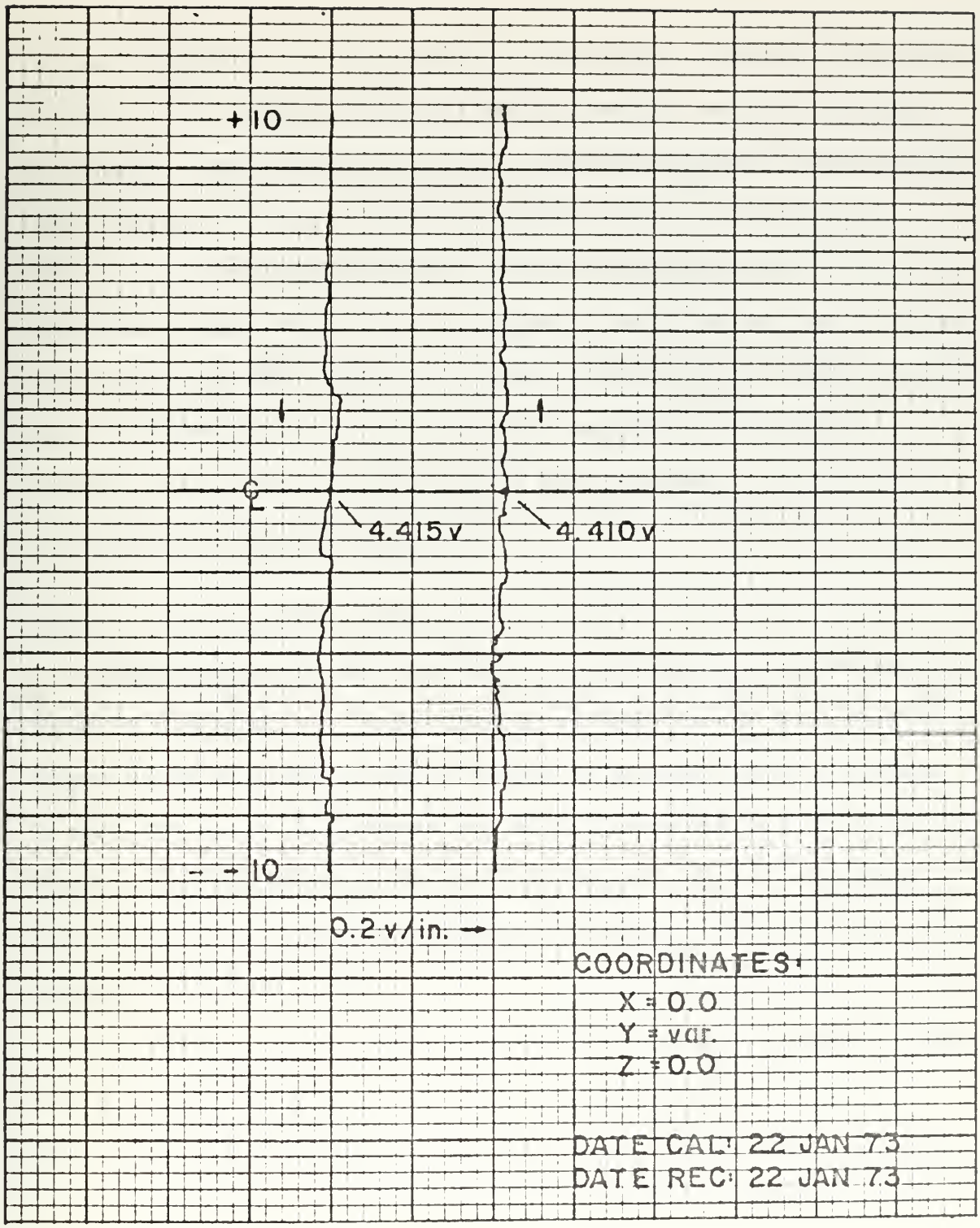

Figure 7. Typical vertical velocity profile at a nominal freestream velocity of 150 ft/sec

constant determined during calibration. Most of the velocity variations in Figure 7 are random, although a one to two foot per second skewness is apparent. The smallest division in Figure 7 represents approximately four feet per second at a nominal velocity of 150 feet per second. Lateral velocity profiles differed little from those in the vertical direction. Longitudinal velocity variation did not exceed two feet per second since the test section walls were compensated for boundary layer growth. The variation of the freestream turbulence intensity as a function of the freestream velocity at the coordinate center of the test section is shown in Figure 8.[2]

TANGENT-OGIVE/CYLINDRICAL MODEL

A single model was used for all of the experiments. Illustrated in Figure 9, the model is a right circular cylinder with a three caliber tangent-ogive nose and an overall length to diameter ratio of fifteen to one. The model was machined from 6061-T6 aluminum to a 16 microinch finish. A circumferential runout of the tangent-ogive nose at three axial stations is presented in Figure 10 showing a maximum total variation of 0.0005 inches.

The internal strain gage balance was inserted into the model using a LC-4 location fit in order to assure adequate contact between the balance sleeve and the model. The balance was positioned and oriented in the model by four pins extending through the model body and flush

---

[2] Complete and detailed test section flow quality information is available upon request to the Department of Mechanical Engineering, Naval Postgraduate School, Monterey, California.

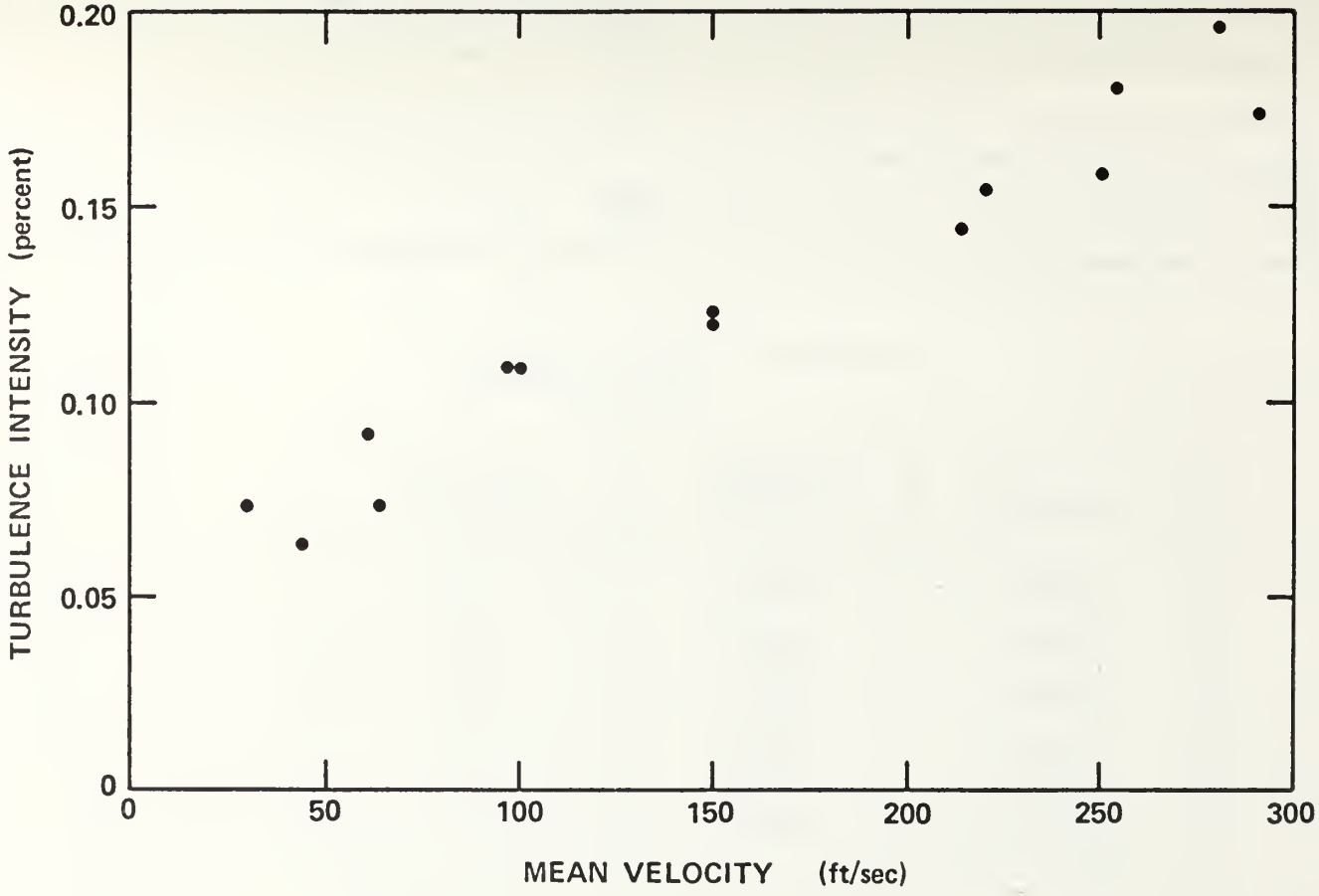

Figure 8. Freestream turbulence intensity at the test section coordinate center

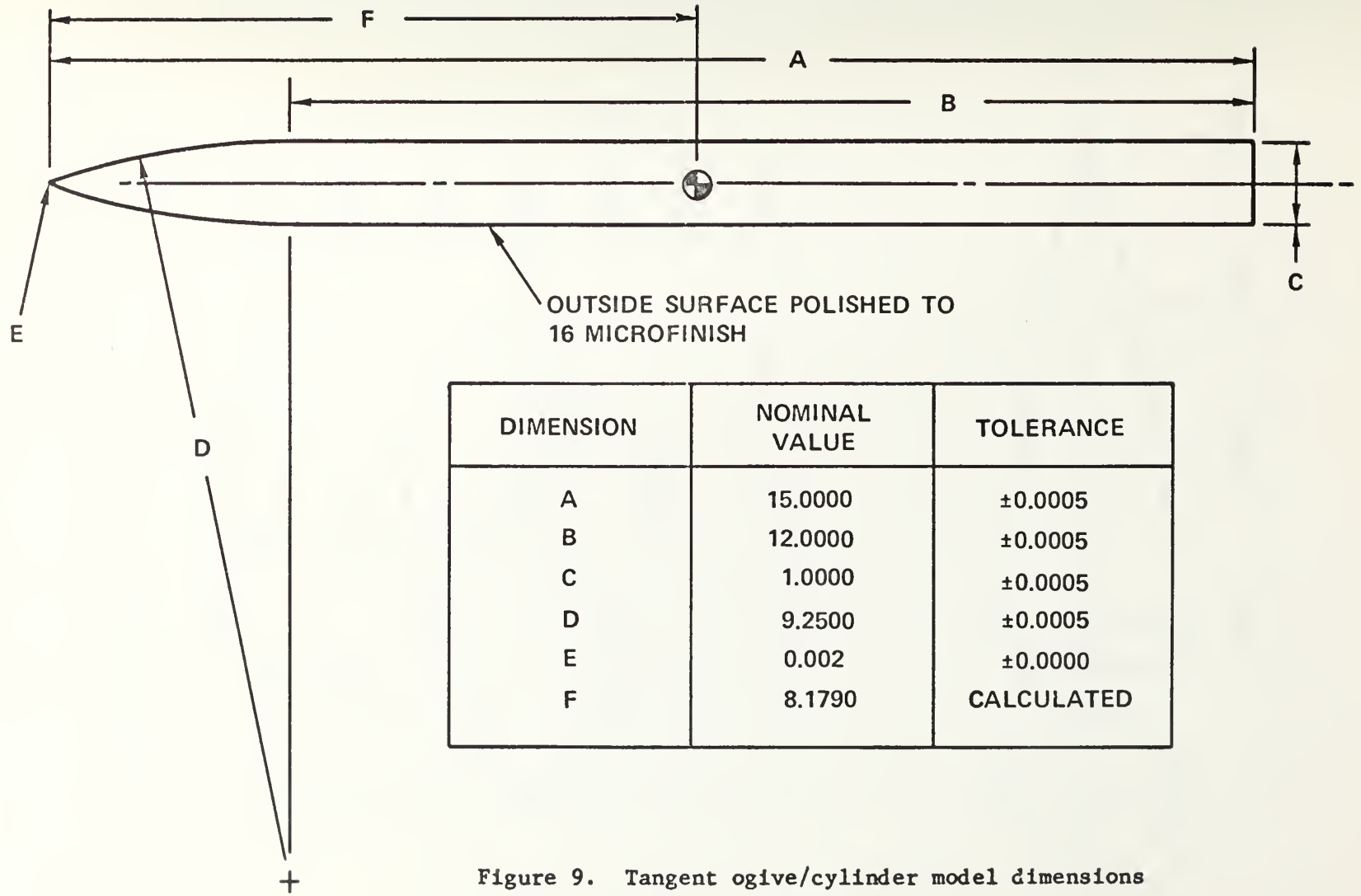

DIMENSION	NOMINAL VALUE	TOLERANCE
A	15.0000	±0.0005
B	12.0000	±0.0005
C	1.0000	±0.0005
D	9.2500	±0.0005
E	0.002	±0.0000
F	8.1790	CALCULATED

Figure 9. Tangent ogive/cylinder model dimensions

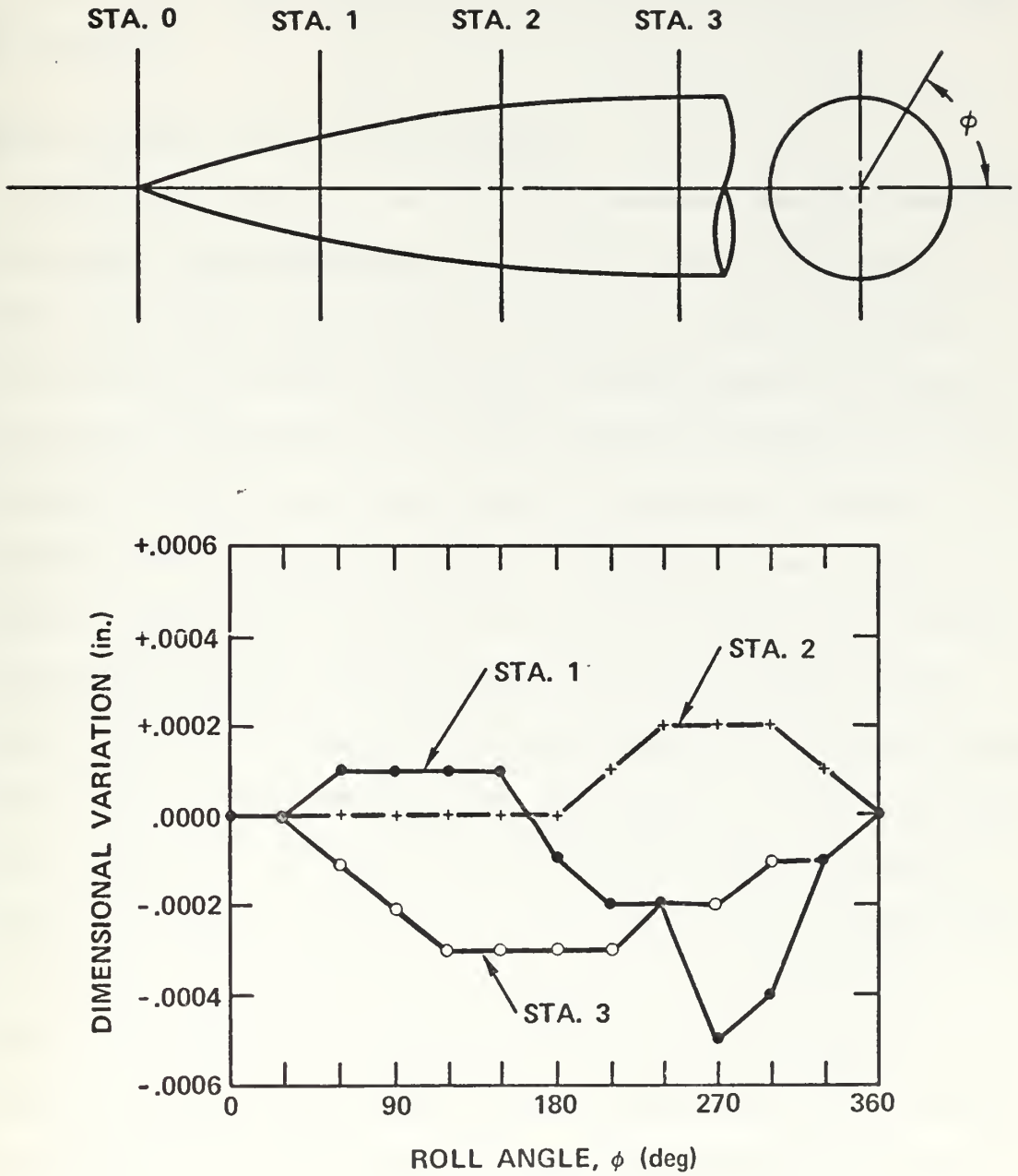

Figure 10. Circumferential runout of the tangent ogive nose

with the outside surface. The balance center of moments coincided with the center of gravity of the model.[3] The balance was rigidly attached to a 0.65 inch diameter stainless steel sting extending from the base of the model.

ANGLE OF ATTACK AND PITCH RATE MECHANISM

The angle of attack, pitch rate and freestream Reynolds number were the primary independent variables during this study. The angle of attack was varied between zero and 90 degrees, while the pitch rate was continuously variable between zero and approximately 300 degrees per second. The rotation of the sting mounted model about its center of gravity at the various pitch rates was accomplished with the mechanism shown in Figures 11 and 12. The mechanism was driven by a ZeroMax QX1-M52 variable speed (0 to 400 rpm) electric motor through an Electroid CB 560 clutch/brake using a six to one speed reducing timing belt link. The clutch/brake output shaft, which extended through seals in the test section side walls, was directly coupled to the yoke shown in Figure 13. The axis of rotation of the mechanism passed through the center of gravity of the model. Opposite the drive-train, the shaft rotated indexing disks to visually display the angle of attack and to operate the control switches. The entire mechanism was vibration isolated from the wind tunnel structure, and after considerable difficulty the drive motor was vibration isolated from the rest of the mechanism. The drive motor speed was set by use of a tachometer,

[3] The model center of gravity was calculated assuming the model was a homogeneous solid body. The center of gravity was located 8.179 inches aft of the apex of the nose.

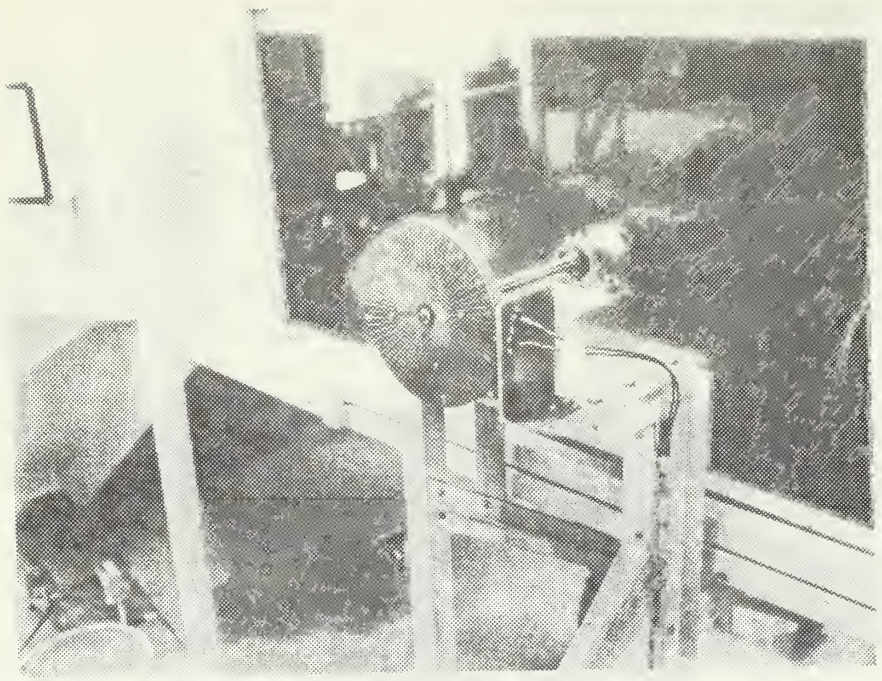

Figure 11. Pitch rate mechanism showing indexing disk and control switches

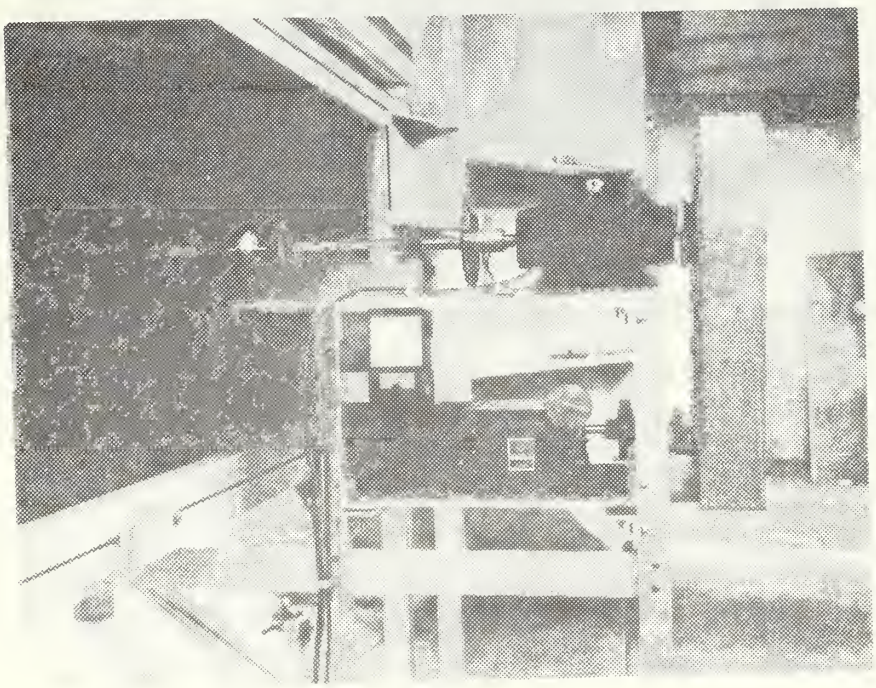

Figure 12. Pitch rate mechanism showing motor, timing belt link and clutch/brake

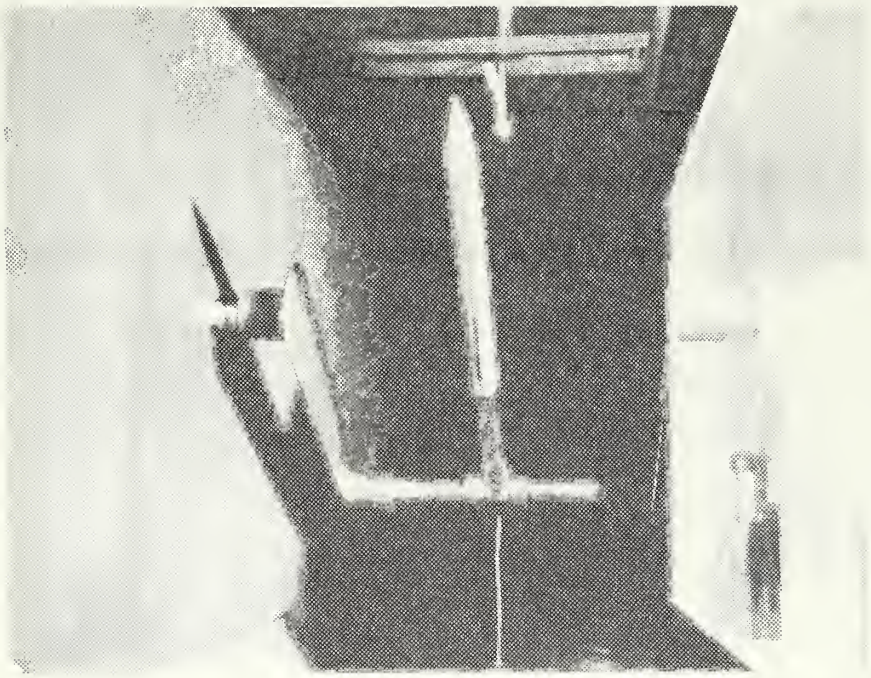

Figure 13. Model and suspension yoke looking downstream

while a potentiometer driven by the clutch/brake output shaft provided an electrical signal directly proportional to the angle of attack.

The drive motor was continuously operated at the selected speed, while the load was clutched in and out. Since the start/stop sequence could not be manually controlled at the higher pitch rates, the control disks provided automatic start/stop pulses. The clutch/brake mechanism was wired so that when the clutch was engaged the brake automatically disengaged and vice versa. A safety device was built into the control disks to prevent the model and yoke assembly from making a full revolution. Timing pulses were generated as the model passed through zero degrees and 90 degrees to facilitate identifying the region of interest on the output record.

In order to assure a constant rate of pitch between zero and 90 degrees a series of tests were conducted to establish the limits of the acceleration phase. Two criteria were satisfied, (1) acceleration to the desired constant angular velocity and (2) no remaining inertial loads as sensed by the normal force gages of the balance. These criteria were not satisfied simultaneously since the balance mechanism was not as heavily damped as the drive mechanism. The starting angle was incrementally increased from -60 degrees to zero degrees at various pitch rates up to the maximum of 300 degrees per second. It was found that the pitch rate assumed a constant value in less than five degrees, but some residual inertial transients were observed for about 12 degrees. It was determined that a starting angle of -15 degrees would be sufficient to attain a constant angular velocity with no remaining inertial loads for all pitch rates. Typical experimental runs were started at -15 degrees and were automatically stopped after the model

passed through 105 degrees, thus the model rotated through a total of 130 degrees but never rotated into a region of flow which had previously been distrubed by the support mechanism.

MEASUREMENT AND RECORDING INSTRUMENTS

Reynolds Number

The freestream Reynolds number was varied solely by variations in the freestream velocity which was variable from approximately 50 to 250 feet per second. Experiments were conducted at nominal velocities of 100, 150 and 250 feet per second. The instantaneous velocity was continuously sensed during the experiments with a DISA 55D01 hot wire anemometer equipped with a DISA 55A22 single wire probe. The anemometer was positioned four inches to the right of the center of gravity coordinates of the model, which were fixed at the test section coordinate origin. The freestream velocity nominally decreased about six percent when the model was rotated due to an increasing pressure drop in the test section. No attempt was made to control these variations since the instantaneous velocity was available for calculating the aerodynamic coefficients. Averaged values of the Reynolds number were used in the presentations that follow. In any given test, the deviation from the average Reynolds number was no more than ± 3 percent.

The anemometer output voltage was recorded on a HP 7700 stripchart recorder via an HP 8801A low gain amplifier. The sensitivity was set so that the voltage could be resolved to $\pm$ one millivolt. Since the velocity is proportional to the fourth power of the anemometer output voltage, at a nominal velocity of 150 feet per second a one millivolt change represents approximately a one percent change in the velocity. Turbulence levels were monitored but not recorded since they differed

little from the earlier surveys. Figure 14 is a block diagram of the entire instrumentation system showing the anemometer probe as item #10.

Angle of Attack

Aerodynamic loads were recorded for angles of attack between zero and 90 degrees; the model, however, was accelerated to the desired constant pitch rate from -15 degrees and decelerated only after passing through an angle of attack of 105 degrees. Angle of attack was continuously recorded as a function of time during a sweep by means of a position potentiometer directly coupled to the clutch/brake output shaft. The angle of attack circuit is schematically illustrated in Figure 14, where item #7 is the sensing potentiometer.

Pitch Rate

The pitch rate mechanism was designed to rotate the sting mounted model about its center of gravity at rates continuously variable from zero to approximately 300 degrees per second. The drive delivered sufficient torque to rapidly accelerate the model and then sustain a constant rate of pitch. The model was rotated through a total angle of no more than 130 degrees during a sweep, so that the supporting yoke never disturbed the flow into which the model eventually rotated. The angular velocity was obtained by computing the slope of the angle of attack versus time trace.

Aerodynamic Loads

The aerodynamic loads experienced by the sting mounted model were measured using a six component floating frame TASK internal

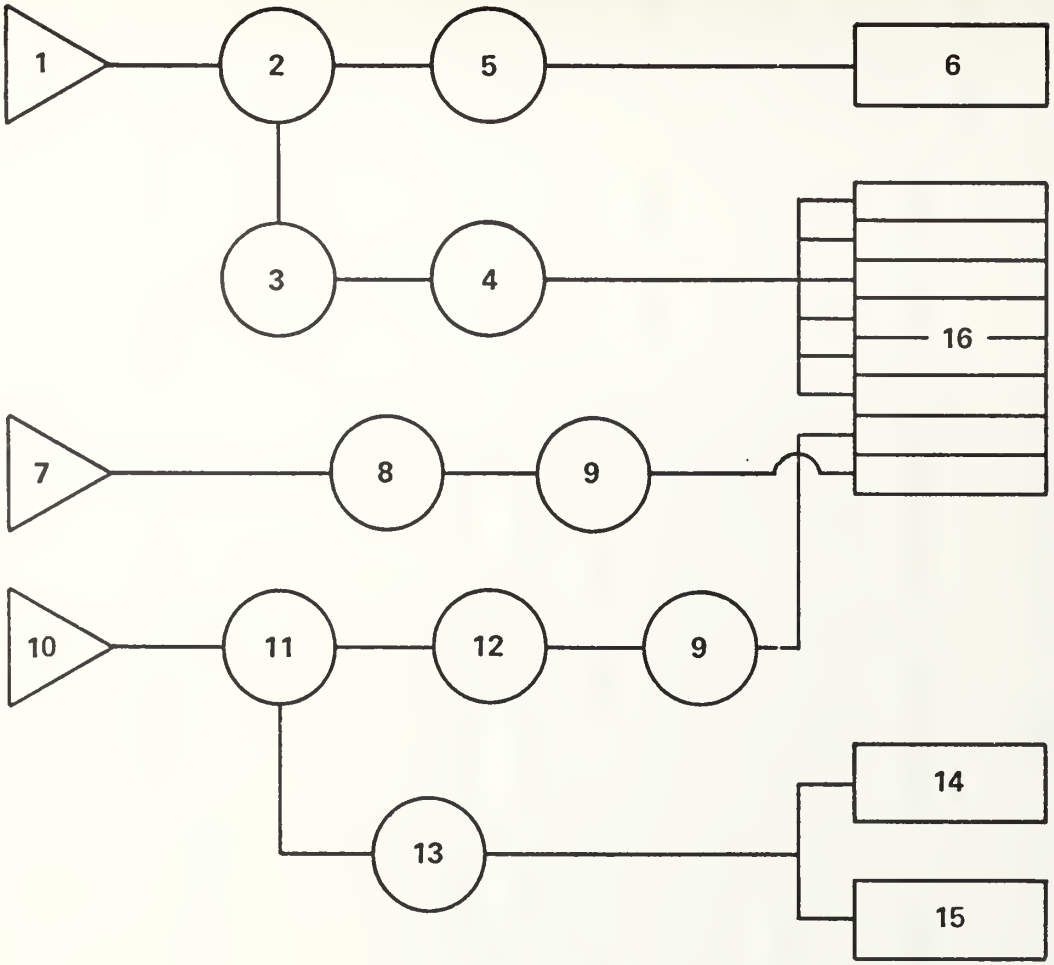

1. TASK six component strain gage balance
2. Power supply and bridge circuit
3. Low pass filter (100cps)
4. HP 8803A low level preamps
5. Six channel switching circuit
6. Simpson 2700 digital voltmeter
7. 1K ten turn potentiometer
8. Power supply and trim circuit
9. HP 8801A low gain amplifier
10. DISA 55A22 single wire probe
11. DISA 55D01 anemometer
12. DISA 55D25 aux. unit (low pass filter, 200cps)
13. DISA 55D25 aux. unit (low pass filter, 5000cps)
14. DISA 55D30 DC voltmeter
15. DISA 55D35 RMS unit
16. HP 7700 eight channel strip chart recorder

Figure 14. Block diagram of the instrumentation system

strain gage balance.[4] This balance, designated HB-2, is commercially available, so a detailed description will not be pursued. The design loads for this balance are:

Normal force, lb.	0 to ±25.0
Yaw force, lb.	0 to ±25.0
Axial force, lb.	0 to ±15.0
Pitch moment, in.-lb.	0 to ±75.0
Yaw moment, in.-lb.	0 to ±62.5
Roll moment, in.-lb.	0 to ±40.0

An analysis of the balance interactions (see Appendix B) lead to the conclusion that the effects of interactions upon the recorded data would not significantly alter the experimental results for the range of loads expected.

The strain gage bridges were excited by a regulated four volt direct current power supply. The bridge output signals were low pass filtered (100 hertz) and fed into the HP 7700 stripchart recorder through HP 8803A low level preamplifiers. The balance circuit is schematically illustrated in Figure 14 where item #1 is the balance. For static measurements the balance bridge output voltages were read directly by use of a six channel switching circuit and a Simpson 2700 digital voltmeter. The sensitivities of the recording instruments were adjusted for the expected loads, where the following ranges and limits of interpretation applied:

---

[4]The HB-2 strain gage balance was on loan from the Naval Ships Research and Development Center, Carderock, Maryland.

Normal aft	-0.50 to 4.50 lb.	±0.02 lb.
Normal forward	-0.50 to 4.50 lb.	±0.02 lb.
Side aft	-2.50 to 2.50 lb.	±0.02 lb.
Side forward	-2.50 to 2.50 lb.	±0.02 lb.
Axial force	-15.0 to 15.0 lb.	±0.20 lb.
Roll moment	-40.0 to 40.0 in.-lb.	±0.4 in.-lb.

These ranges correspond to full scale deflections of the stripchart galvonometers. The interpretation tolerances correspond to a quarter of the smallest division on the chart paper.

GENERAL EXPERIMENTAL PROCEDURE

The experiments fell into two categories, those at a fixed Reynolds number while varying the pitch rate and those at a fixed pitch rate while varying the Reynolds number. The first series of experiments were conducted at a Reynolds number of $8X10^4$ while the pitch rate was varied between zero and approximately 300 degrees per second. The second series, at fixed pitch rates, was conducted at Reynolds numbers of $5X10^4$ and $1.4X10^5$. Throughout the experiments specific tests were conducted to verify the reproducibility of the data. These checks provided for early recognition of potential instrumentation inadequacies, and improved the confidence with which trends could be identified.

EXPERIMENTAL RESULTS AND DISCUSSION

The experimental results are presented in two sections; (1) static aerodynamics and (2) aerodynamics while undergoing a uniform pitching motion. The static aerodynamic data provide a baseline from which the effects of pitch rate can be adjudged in terms of increments to the aerodynamic coefficients. The implications of the flow visualization studies will be incorporated into both sections.

STATIC AERODYNAMICS

Normal force, pitching moment, yaw force and yaw moment were recorded at five degree increments of the angle of attack between zero and 90 degrees. The test conditions were allowed to stabilize at each angle before recording the forces. Three series of experiments were conducted for nominal freestream Reynolds numbers of $5X10^4$, $8X10^4$ and $1.4X10^5$. These Reynolds numbers were somewhat less than a critical crossflow Reynolds number of about $2X10^5$, and therefore should be considered subcritical throughout the angle of attack range. The low turbulence level within the wind tunnel test section provides additional justification for assuming that the flow was subcritical for all test conditions considered.

The static aerodynamic force and moment coefficients and the center of pressure are presented in Figures 15 to 19 for the three values of the freestream Reynolds number. The continuous curve represents a best fit to the experimental data for the Reynolds number $8X10^4$. Experimental errors, uncertainties and reproducibility of the experimental data are discussed in Appendix C, where it is concluded

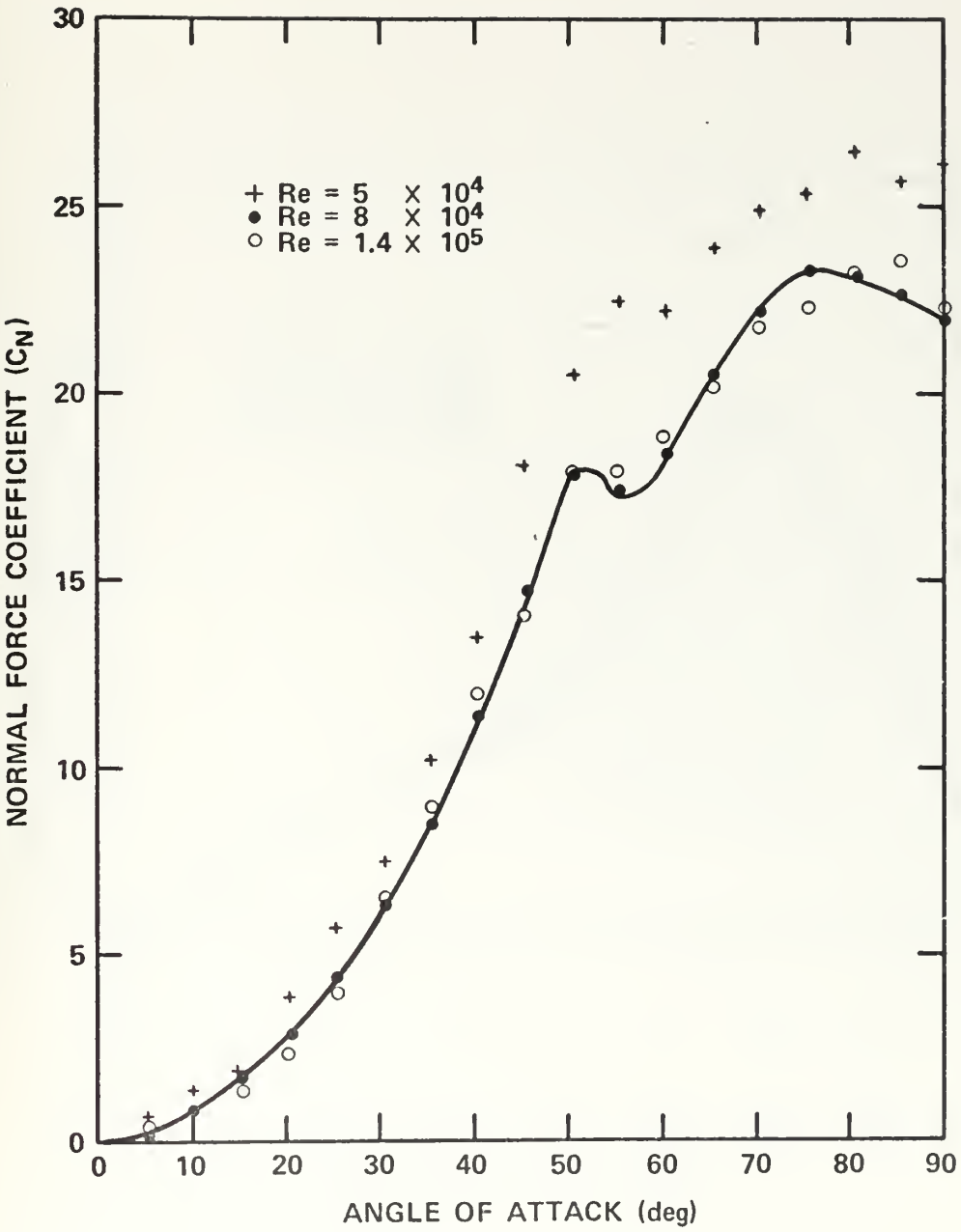

Figure 15. Static normal force coefficient variation with angle of attack for various Reynolds numbers

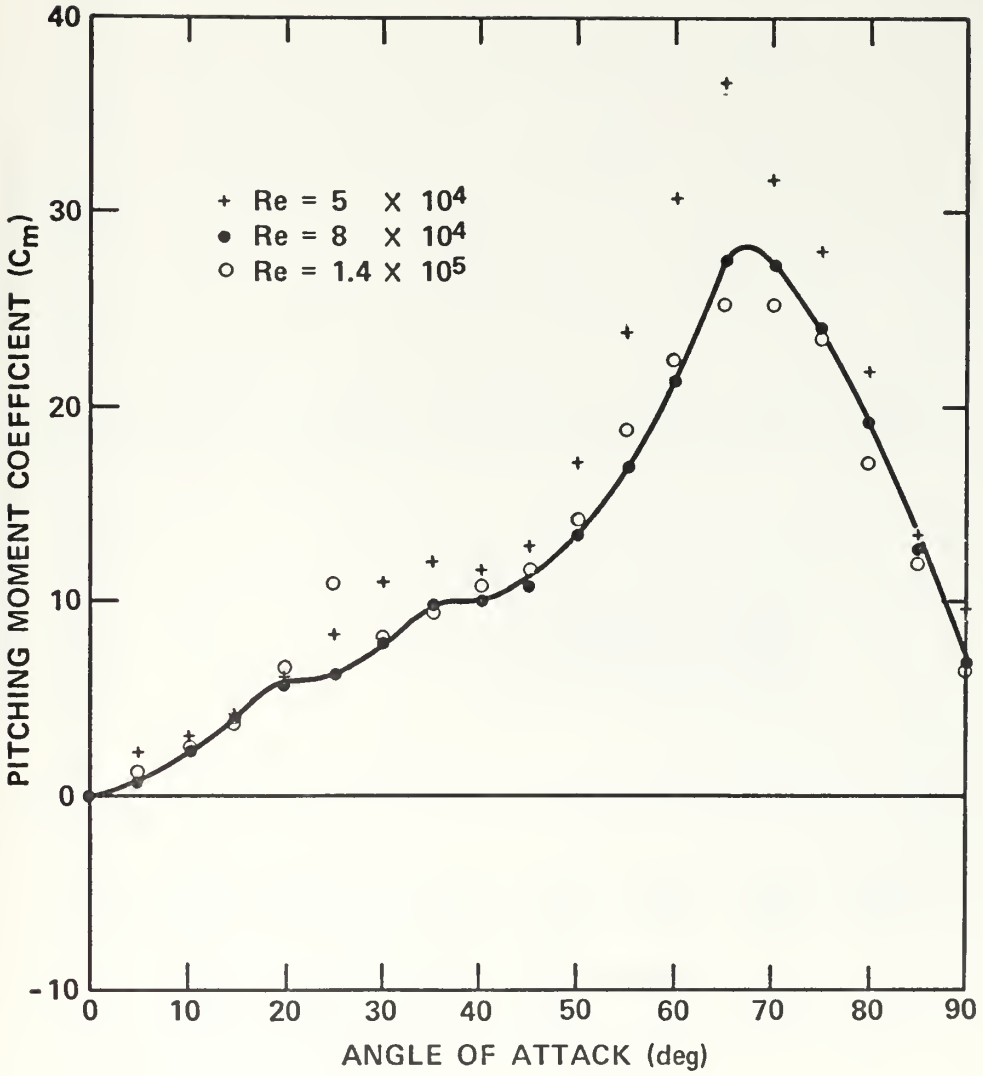

Figure 16. Static pitching moment coefficient variation with angle of attack for various Reynolds numbers

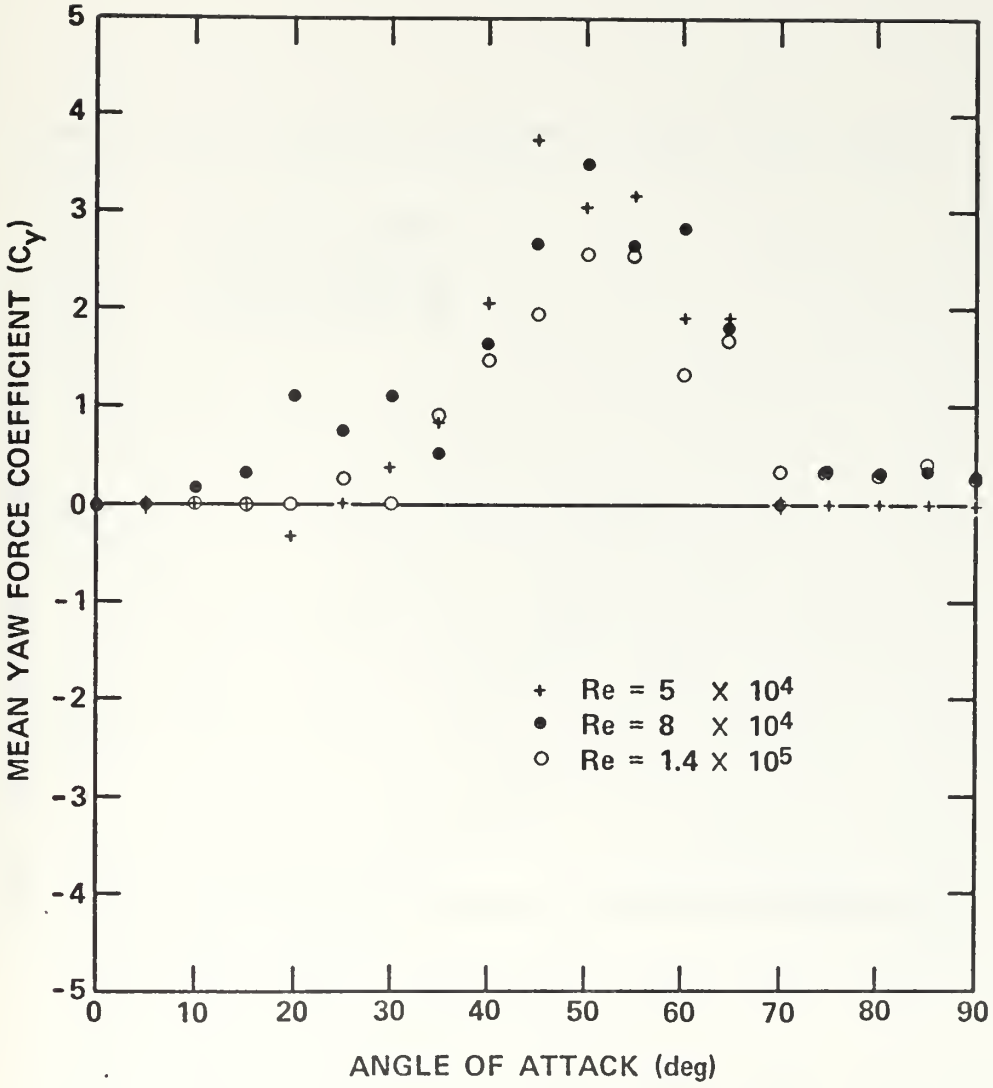

Figure 17. Static mean yaw force coefficient variation with angle of attack for various Reynolds numbers

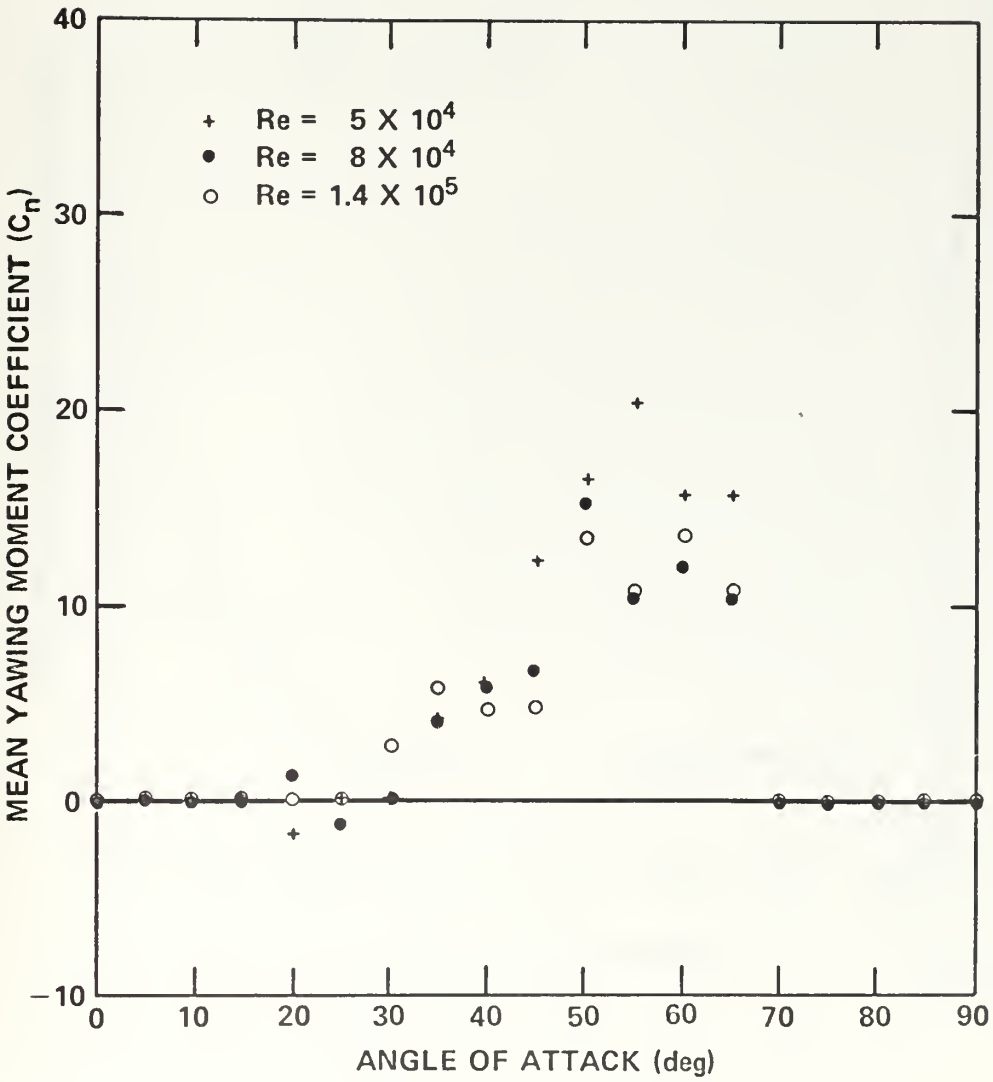

Figure 18. Static mean yawing moment coefficient variation with angle of attack for various Reynolds numbers

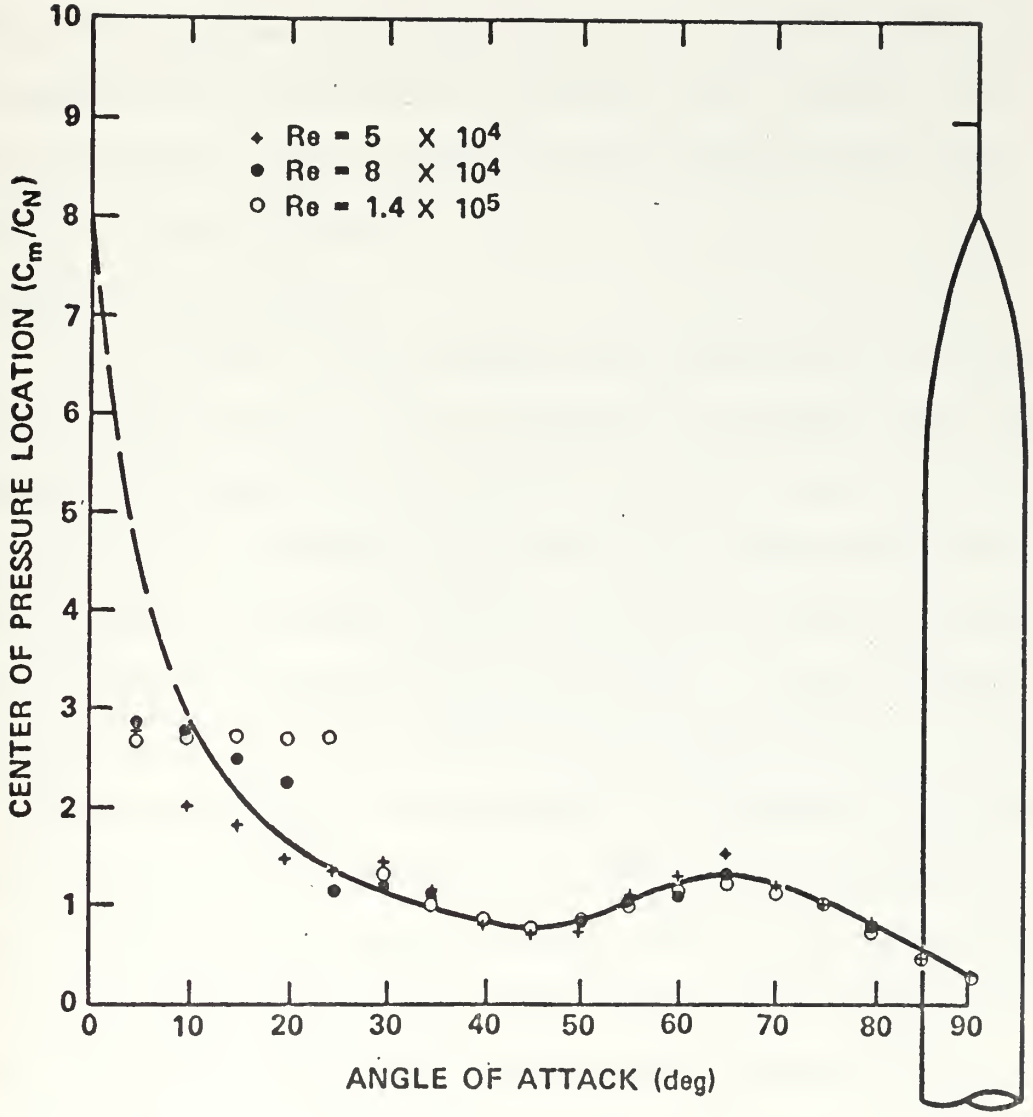

Figure 19. Static center of pressure location variation with angle of attack for various Reynolds numbers

that an uncertainty band of no more than ± 0.4 in the normal force and pitching moment coefficients should be associated with these data throughout the angle of attack range. Additional checks on the validity of the present experimental data are provided in Appendix D. The magnitude of the normal force coefficient agrees favorably with referenced data when angle of attack, length-to-diameter ratio and Reynolds number are considered.

Reynolds Number Effects

The aerodynamic loads developed on an inclined body of revolution are strongly dependent upon the separation of boundary layer fluid which feeds into regions of concentrated vorticity. Since the boundary layer thickness is inversely proportional to the square root of the Reynolds number, increasing the Reynolds number decreases the boundary layer thickness at a given position on the wall. A thinner boundary layer decreases the tendency toward separation since $(\partial u/\partial y) \sim 1/\delta$, and for separation $(\partial u/\partial y)_{wall} = 0$ for steady flow. Therefore, the point of separation shifts toward the leeside of the body with increasing Reynolds number as long as the flow remains laminar [Ref. 14]. As the point of separation moves farther toward the leeside of the body, the form drag (normal force) is decreased as a consequence of a greater pressure recovery on the leeside of the body [Ref. 15]. The data presented in Figure 15 is in accordance with these arguments, showing a larger normal force coefficient for $R_e = 5X10^4$ than for either $8X10^4$ or $1.4X10^5$. Considering the stated uncertainty band, the normal force coefficient at the two larger values of the Reynolds number are nearly indistinguishable implying that the point of separation has moved a negligible amount further aft for the increase in the Reynolds number.

It should be noted that the Reynolds numbers under discussion are freestream values based on the maximum body diameter. The local crossflow Reynolds number will be less than the freestream value by the sine of the angle of attack for all stations along the body, and even less along the nose due to the reduced diameter. Depending upon the configuration of the wake vortices and the freestream turbulence, the separation angle can vary from approximately 80 to 110 degrees from the front stagnation point for local Reynolds numbers between 10^3 and 10^5, [Ref. 16], which is sufficient to cause the observed results.

Normal Forces

The normal force coefficient smoothly increases with increasing angle of attack between zero and about 50 degrees. Between 50 and 60 degrees there is an apparent stall and subsequent recovery. Beyond this region of apparent stall, there is a loss of normal force attributed to an adjustment of the aerodynamic loads to compensate for the changing distribution of frontal area where the crossflow dominates.

The existence of the inflection in the normal force coefficient curve at about 55 degrees was first reported in Ref. 17. In Ref. 17 the same phenomenon was observed for both cone/cylinders and ogive/cylinders, and was attributed to flow unsteadiness during a transition from a flow dominated by the axial component to a flow in which the crossflow component dominates. Support for this argument was obtained during the flow visualization studies (see Figure 29 through Figure 34,

Appendix A). Also, during the pitch rate experiments, continuous normal force records show an unsteady normal force response in the region of 50 to 60 degrees angle of attack (see Figure 20a).

The pitching moment curve is relatively uneventful with the exception of some rather small deviations between about 20 and 40 degrees angle of attack. There is no correlation between the deviations on the pitching moment curve and the inflection on the normal force curve. In the angle of attack range in which the deviations in the pitching moment occur, the wake can be characterized by periodic asymmetric vortex shedding [Ref. 18]. Assuming the first trailing vortex breaks away from the body at the shoulder of the nose, the spacing between trailing vortices of like sign can be calculated using the equation developed in Ref. 18; that is

$$2g = \frac{d \cos \alpha}{S}$$

Calculating the spacing between trailing vortices at an angle of attack of 20 degrees yields g = 6.87d. Thus, measuring the spacing from the shoulder of the nose, one or maybe two trailing vortices would exist on the 12d long afterbody. At an angle of attack of 40 degrees the spacing between trailing vortices becomes g = 2.98d, and at least four trailing vortices would be expected. The point is, in the angle of attack region of periodic asymmetric vortex shedding, additional trailing vortices emanate from the base of the body with increasing angle of attack. The addition of trailing vortices at the base of the body has two effects; (1) to increment the total normal force and (2) to cause a redistribution of the normal force. The incrementing of the normal force appears to be smooth (see Figure 15), whereas the

redistribution of the normal force causes the deviations in the pitching moment. This description of the deviations in the pitching moment is illustrated in the motion picture film taken during the flow visualization studies. The continuous side force records presented in Figure 20b also illustrate the development of additional vortices near the base of the body with increasing angle of attack. Note that a positive side force is developed at the aft gage at about 20 degrees, where no side force is apparent on the forward gage. With increasing angle of attack the side force aft record changes sign, indicating that one new vortex trail is now emanating from the base, thereby shifting the asymmetry in the wake vortex pattern.

Yaw Forces

The occurrence of a net yaw force at about 17 degrees (see Figure 17 and Figure 20b) is consistent with data presented in the literature for the beginning of asymmetric vortex shedding. Asymmetric shedding of discrete trailing vortices continues with increasing angle of attack until approximately 52 degrees. At this angle of attack the periodic shedding becomes unstable and the magnitude decays. At about 68 degrees the mean value (time averaged) of the fluctuating yaw force becomes zero (see Figure 20b). The variation in the angle of attack at which asymmetric vortex shedding first occurred during these experiments was six degrees on either side of the 17 degree mean value. Reynolds number effects are almost totally obscured in the yaw data due to their highly transient character.

Center of Pressure Location

The scatter of the center of pressure data, presented in Figure 19, at the low angles of attack should be disregarded since these

values are obtained by dividing a small pitching moment by an even smaller normal force, and any slight error is tremendously magnified in the center of pressure location. As was to be expected, the effect of Reynolds number upon the center of pressure location was small since the center of pressure is merely a ratio of aerodynamic loads, both of which are dependent to nearly the same extent upon the Reynolds number.

At zero angle of attack the clean axisymmetric body develops no lift. For small angles of attack the nose contributes a majority of the normal force as a result of the acceleration of the axial flow over the expanding nose. The center of pressure moves further aft from the apex with increasing angle of attack as the afterbody begins contributing more to the normal force due to the formation of wake vortices. Between 40 and 50 degrees the center of pressure location reaches a temporary minimum, then moves forward until about 65 degrees. As the angle of attack is further increased the center of pressure approaches a position consistent with the center of the presented frontal area at 90 degrees. The temporary forward movement of the center of pressure indicates a loss of normal force on the aft portion of the body. This trend appears to be coupled to the inflection in the normal force curve at about 55 degrees (see Figure 15). As discussed earlier, the inflection is the result of a transition from a flow dominated by the axial component to a flow dominated by the crossflow component. In the region of the nose this transition is delayed until a higher angle of attack is reached so that the center of pressure moves forward. This persistence of the nose generated vortex at high angles

was dramatically illustrated during the flow visualization studies (see Figure 30 through Figure 33, Appendix A).

A curve drawn point to point in Figure 19 would include small deviations from the smooth curve shown at angles of attack of 20 and 40 degrees. These small deviations in the center of pressure location would be the result of the similar deviations in the pitching moment. The irregularities in the pitching moment are most likely a consequence of additional vortices emanating from the base of the body, as was discussed in the section on the normal force.

AERODYNAMICS WHILE UNDERGOING A UNIFORM PITCHING MOTION

The model was accelerated to the desired angular velocity from -15 degrees, then maintained at a constant angular velocity between zero and 90 degrees, and decelerated in another 15 degrees. The normal force, pitching moment, yaw force and yaw moment were continuously recorded as functions of time, as was the angle of attack. Actual pitch rates were computed from the slope of the angle of attack versus time trace. Experiments were conducted using drive motor speed settings of 10, 20, 50, 100, 200, and 300 revolutions per minute, which is roughly equivalent to the model angular velocity in degrees per second due to the six to one speed reduction in the drive train.

Typical stripchart records are presented in Figure 20. The basic character of these traces was similar to that for all of the pitch rates investigated. Figure 20a represents the output of the fore and aft normal force load cells; Figure 20b represents the output of the two side force load cells; Figure 20c represents the traces for the

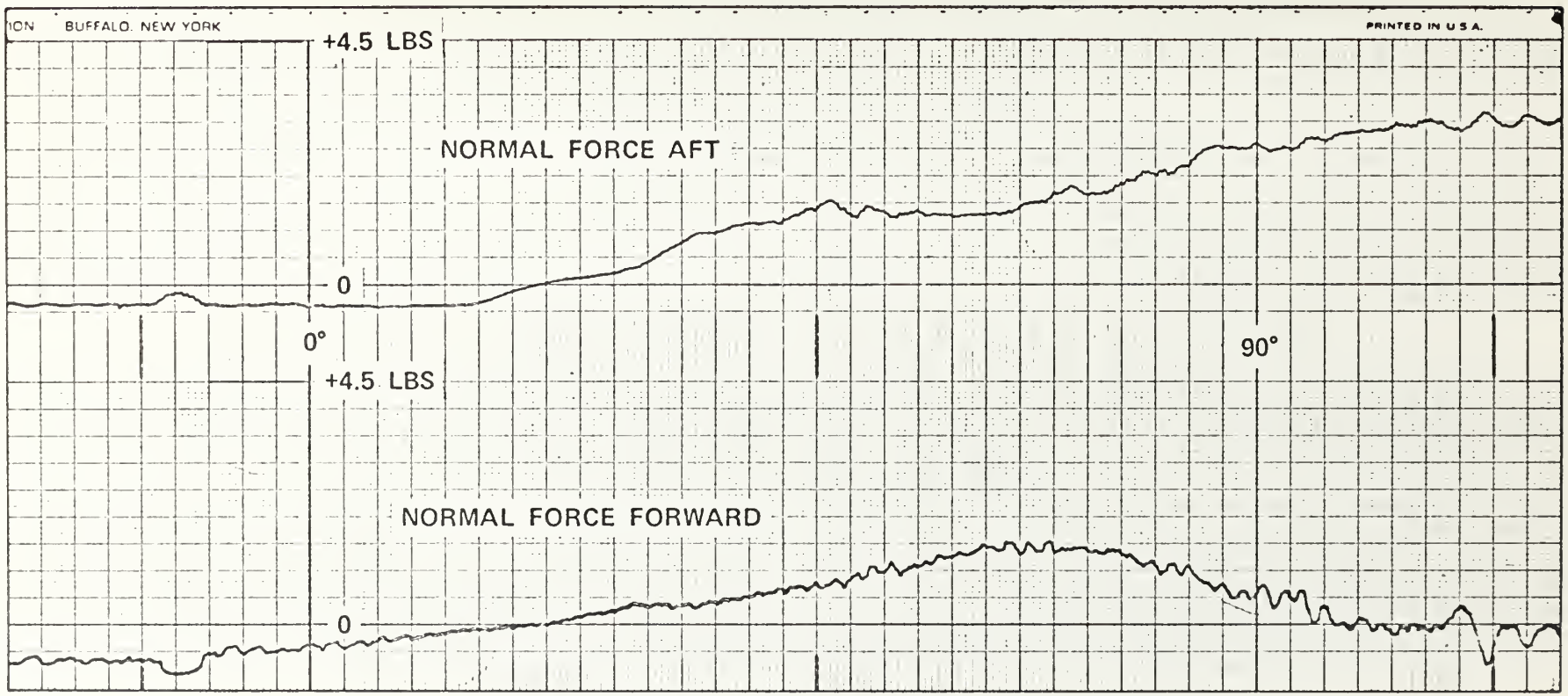

Figure 20a. Typical stripchart record for nominal freestream velocity of 150 ft/sec and pitch rate of 50 deg/sec

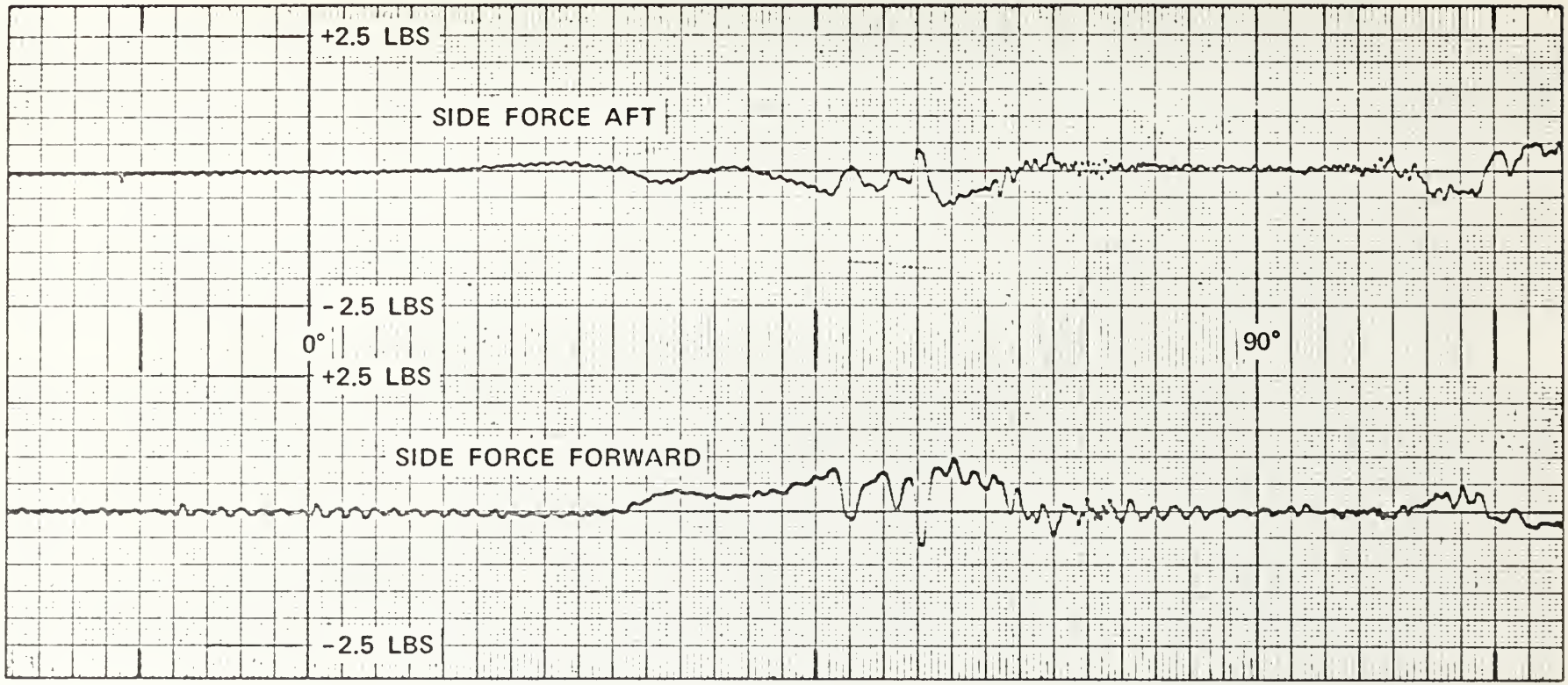

Figure 20b. Typical stripchart record for nominal freestream velocity of 150 ft/sec and pitch rate of 50 deg/sec

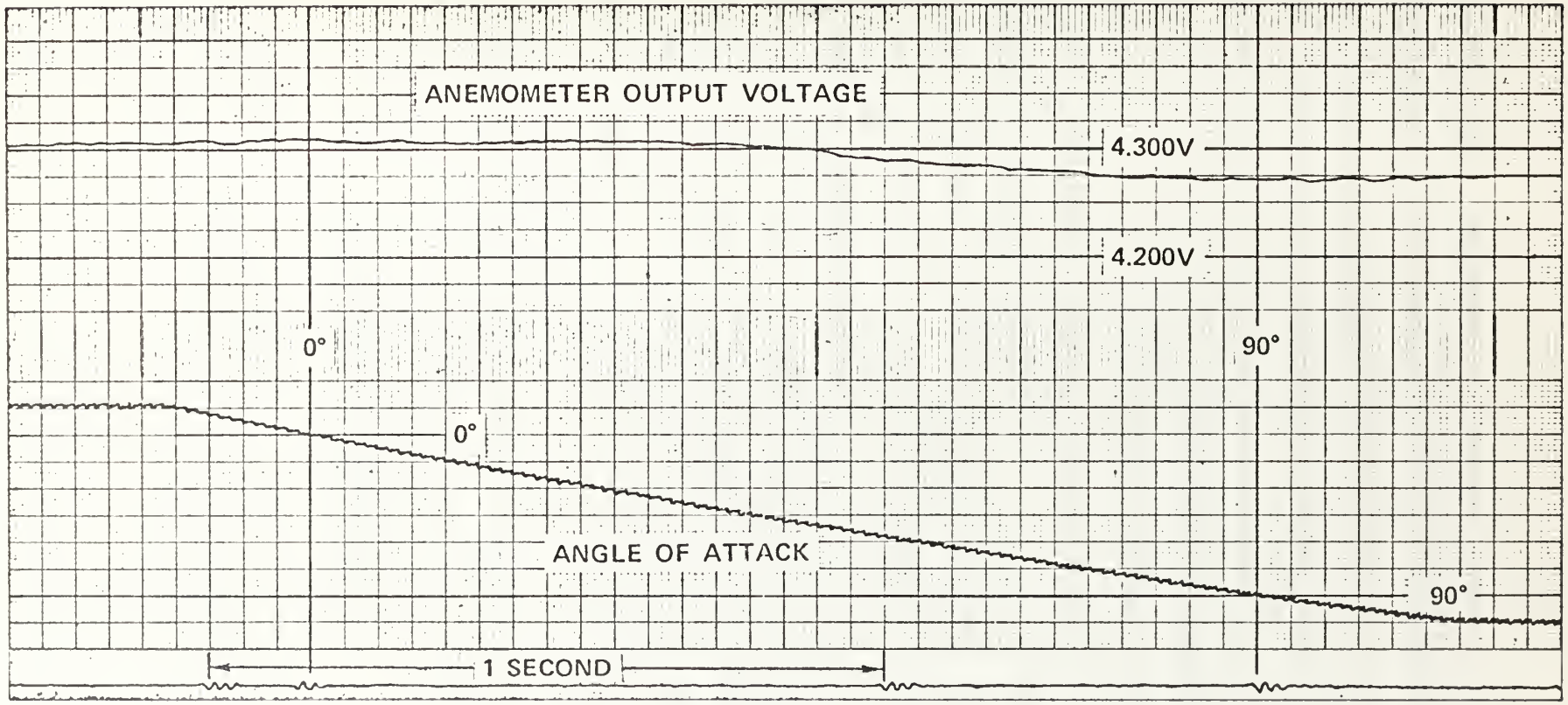

Figure 20c. Typical stripchart record for nominal freestream velocity of 150 ft/sec and pitch rate of 50 deg/sec

anemometer output voltage and the angle of attack potentiometer. The scales indicated on the stripchart are only approximate since nonlinear weight corrections and nonunity scale factors have not been included.

The normal force forward gage was always the first to respond with increasing angle of attack, then as the center of pressure moved further aft the normal force aft gage began to respond. The normal force at both gage stations continues to increase with angle of attack until about 55 degrees, at which point the normal aft gage experiences a loss while the normal force forward continues to increase to a maximum near 65 degrees. Beyond this angle of attack the total normal force was adjusting to the changing distribution of frontal area in the region of crossflow dominance.

Net side forces were detectable as early as about 15 degrees. These early occurring side force variations were relatively smooth up to an angle of about 55 degrees, where they became very erratic. This erratic behavior persisted for approximately 15 degrees, then the net side force vanished.

Freestream velocity variations were computed from the recorded anemometer output voltage variations using the following expression

$$\delta V = 4E\left(\frac{E^2 - E_0^2}{\beta^2}\right)\delta E$$

which is simply the derivate of the governing anemometer voltage/velocity relation. The variation in velocity corresponding to the 0.045 volt variation shown in Figure 20c is less than six percent of the mean value of 150 feet per second. The velocity variations were even less than this value for the higher rates of pitch since the wind tunnel response time to the changing pressure drop was much longer than the

total sweep time. No attempt was made to reduce or eliminate this transient since it was relatively small, and the instantaneous velocity was available for use in the coefficient determinations.

The slight curvature of the angle of attack trace was due to the nonlinear output of the potentiometer used to indicate the angle of attack. This nonlinearity was corrected in the data reduction scheme. Timing marks were used to indicate when the model actually passed through zero and 90 degrees.

Reynolds Number of 80,000

Pitch rate experiments were conducted at a nominal freestream Reynolds number of $8X10^4$. The effects of pitch rate will be illustrated with the normal force and pitching moment coefficients.

Figure 21 shows how the normal force coefficient at various rates of pitch compares with that for the truly static case (continuous curve). Considering an uncertainty band of ± 0.4 in the normal force coefficient throughout the angle of attack range, it is easily seen that pitch rates of 10.8 and 21.8 degrees per second are not significantly different from the static data, at least up to 50 degrees angle of attack. Beyond 50 degrees the difference may be sufficient to indicate some consistent pitch rate dependence. At an angular velocity of 49.5 degrees per second the normal force coefficient is fairly easily distinguished from the static data throughout the angle of attack range. A curve representing the data for this pitch rate would have a steeper slope (C_{N_α}) and would reach the inflection point at a slightly higher angle of attack. The normal force coefficient is higher at the inflection and the transition appears to be more gradual than occurs in the static case. These trends were repeatable

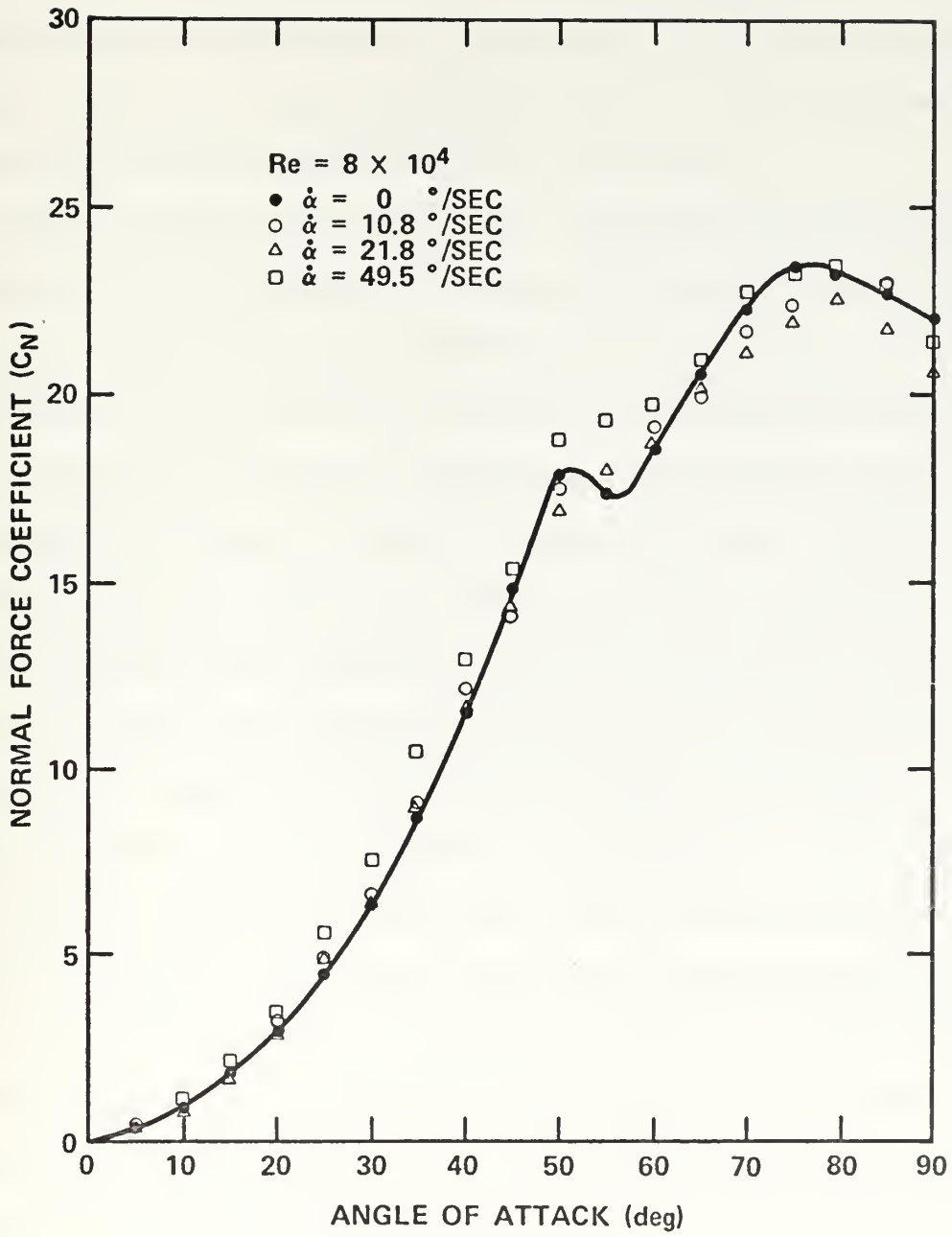

Figure 21. Normal force coefficient variation with angle of attack for various pitch rates

over an extensive series of corroborative tests. From Figure 21 it can be concluded that rates of pitch less than 20 degrees per second are relatively indistinguishable from static data. For pitch rates greater than 20 degrees per second consideration must be given to the rate of pitch when interpreting the normal force coefficient.

Figure 22 compares the normal force coefficients for angular velocities of 95.3, 186.3 and 281.3 degrees per second with those for zero pitch rate. The trends established for 49.5 degrees per second are supported by the data for 95.3 and 186.3 degrees per second; that is, an increasing coefficient magnitude at a given angle of attack and a shifting of the angle at which the inflection occurs. However, with a further increase in the angular velocity to 281.3 degrees per second the coefficient magnitude decreases, and the angle at which the inflection occurs nearly returns to the value for the static case. A discussion of this trend reversal will be delayed until later, where a constant pitch rate parameter is discussed.

Figure 23 shows the pitching moment coefficient for the same angular velocities. The maximum value of the pitching moment coefficients and the general shape of the curves remain relatively independent of pitch rate, although the angle of attack at which the maximum occurs decreases with increasing pitch rate. Again, at 281.3 degrees per second the trend is reversed.

The center of pressure curve, presented in Figure 24, illustrates the similarity of the normal force and pitching moment curves at the various rates of pitch to those for zero pitch rate. The data for nonzero pitch rates falls on essentially the same curve as the static data up to about 75 degrees. The divergence of the data above an

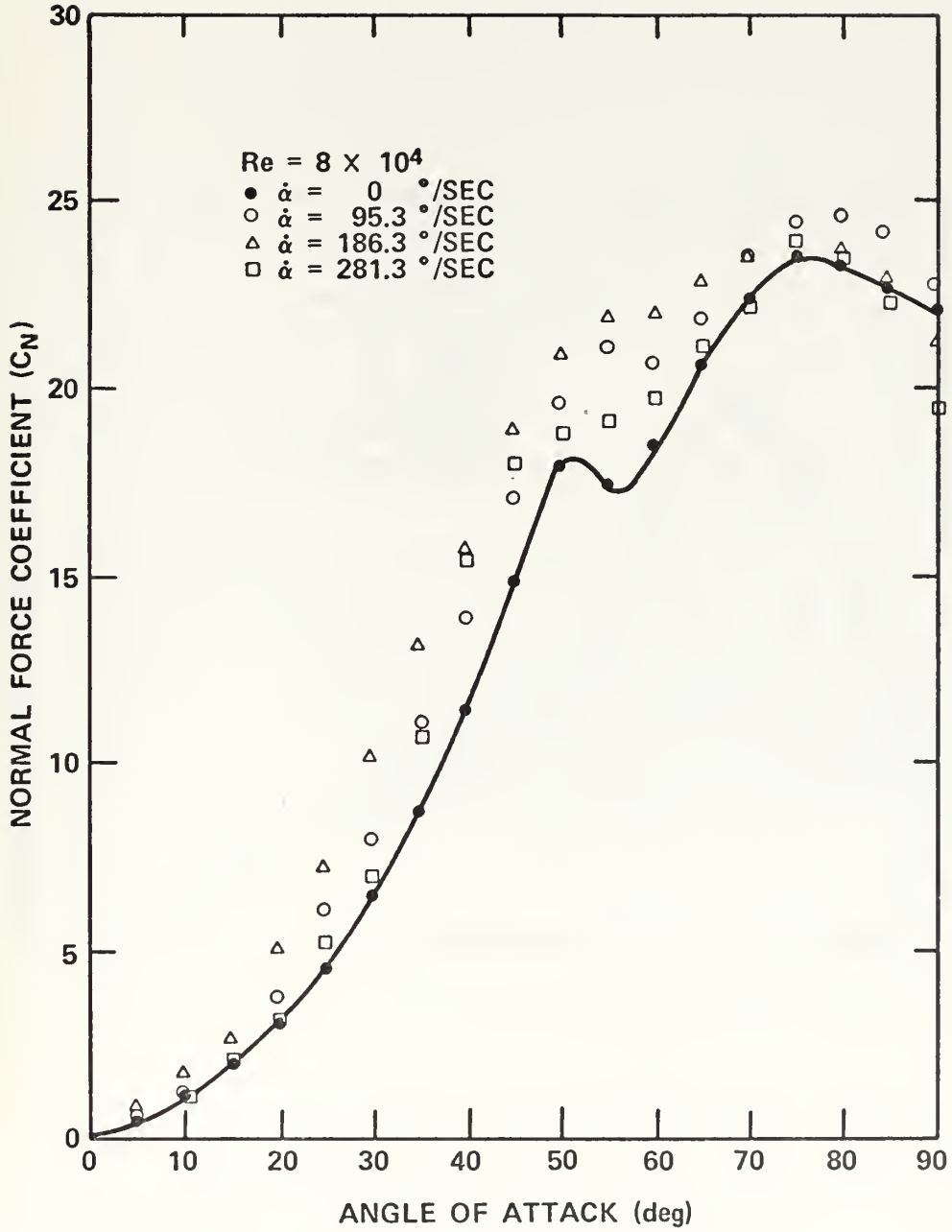

Figure 22. Normal force coefficient variation with angle of attack for various pitch rates

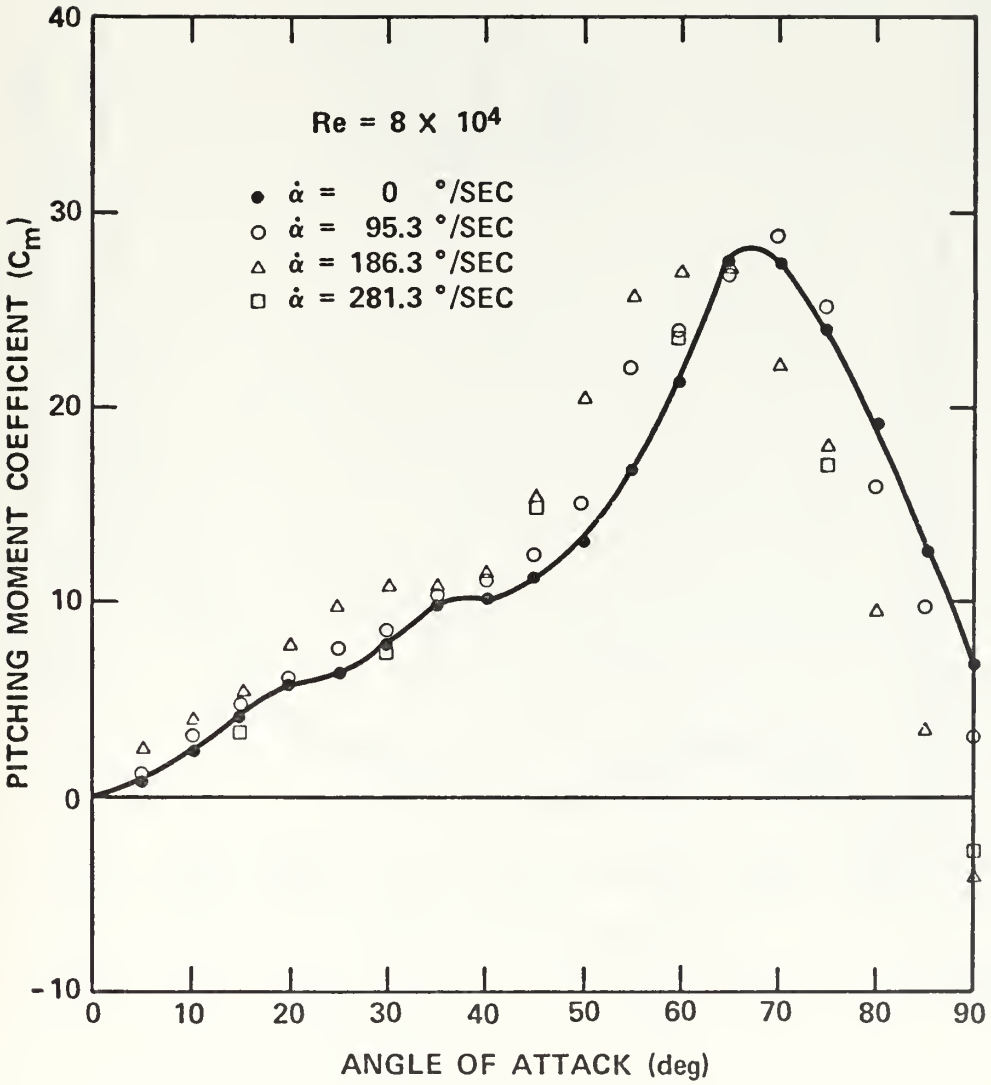

Figure 23. Pitching moment coefficient variations with angle of attack for various pitch rates

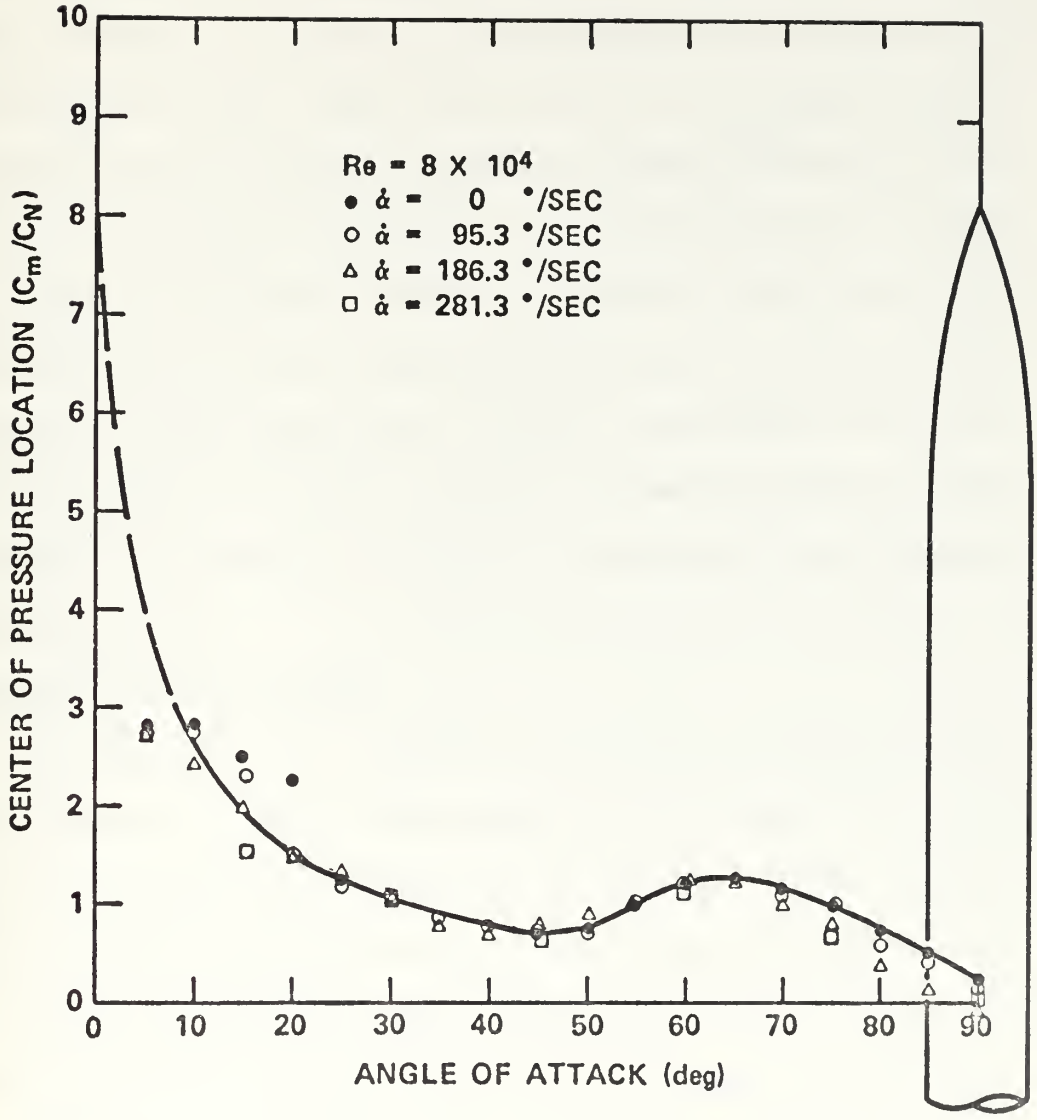

Figure 24. Center of pressure location variation with angle of attack for various pitch rates

angle of 75 degrees indicates a more rapid adjustment of the normal force to the distribution of the frontal area with increasing rates of pitch. The more rapid adjustment with increased pitch rate is also apparent in Figure 23, where the pitching moment decays more rapidly for the higher pitch rates. These results may be a consequence of the experimental set-up; that is, in these experiments the center of the frontal area presented at an angle of attack of 90 degrees coincides with the axis of rotation. Referring to Figures 21 and 22, the normal force coefficients for all pitch rates converge on the static value for angles of attack above about 75 degrees. Therefore, it is suggested that pitch rate effects apparent in these data above an angle of attack of 75 degrees are, in fact, a consequence of the particular experimental set-up.

Reynolds Number of 50,000

Another test of the effects of pitch rate was conducted at a Reynolds number of $5X10^4$ for essentially the same values of the pitch rates used during the experiments conducted at $R_e = 8X10^4$. Figure 25 shows the normal force coefficient for the various pitch rates. At this value of the Reynolds number the pitch rate appears to have little effect upon the normal force. This result indicates that variations due to pitch rate are closely coupled to the Reynolds number. The effects of pitch rate may only be apparent if the rate of pitch induces a local velocity increment at a station where the crossflow Reynolds number would otherwise remain at a threshold to some change in the separation angle, boundary layer transition, or change in the wake vortex configuration.

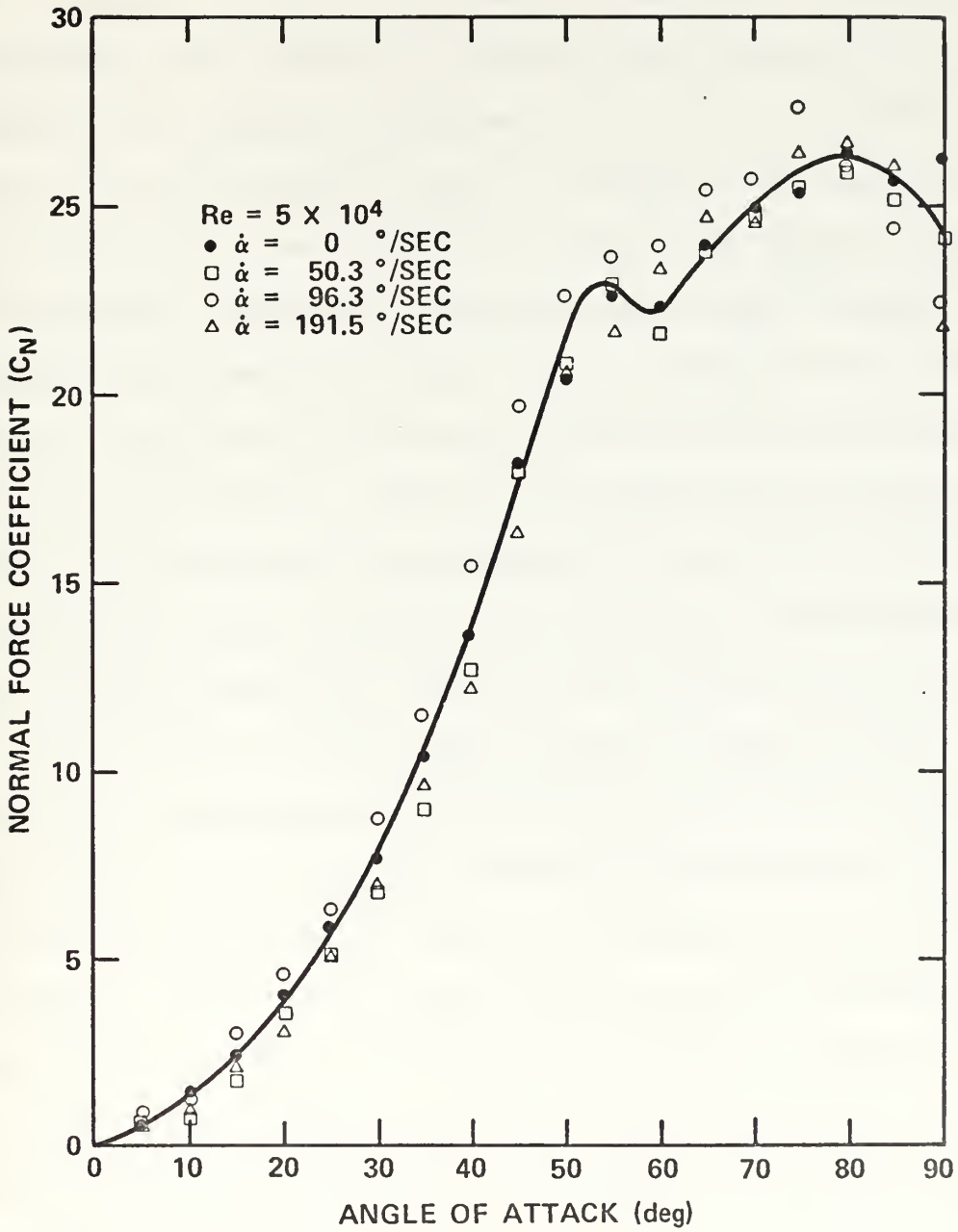

Figure 25. Normal force coefficient variation with angle of attack for various pitch rates

Constant Pitch Rate Parameter

A final sequence of experiments was conducted to determine if the Reynolds number effects at a constant value of the pitch rate parameter, $\dot{\alpha}d/V_o$, would be consistent with the pitch rate trends established at a Reynolds number of $8X10^4$. Experiments were conducted for a value of the pitch rate parameter of $2.7X10^{-3}$ for Reynolds numbers of $5X10^4$ and $8X10^4$. The normal force coefficients obtained during these experiments are presented in Figure 26. A comparison of the continuous curves for zero pitch rate and the data points for the same nonzero pitch rate are consistent. That is, the normal force coefficient at the lower Reynolds number is greater than the normal force coefficient for the higher Reynolds number for both a zero and a nonzero pitch rate. Further examination of Figure 26 illustrates the insensitivity of the normal force to pitch rate at a Reynolds number of $5X10^4$. However, the data indicates that increasing pitch rate may have an overall effect of decreasing the freestream Reynolds number, at least at the lower angles of attack. That is, at low angles of attack, the data for $\dot{\alpha}d/V_o = 2.7X10^{-3}$ and $R_e = 8X10^4$ (the open circles in Figure 26) appears to fall on the $R_e = 5X10^4$ curve. The effect of pitch rate is to decrease the local crossflow velocity on that portion of the body forward of the axis of rotation while increasing the crossflow velocity aft of the axis of rotation. Although for the angular velocities investigated the maximum change in velocity induced by pitch rate was less than three feet per second, the net effect is to reduce or disturb the crossflow Reynolds number near the apex where the wake vortex configuration is established for the entire body. This disturbance of the crossflow Reynolds number on the nose appears to cause an increase

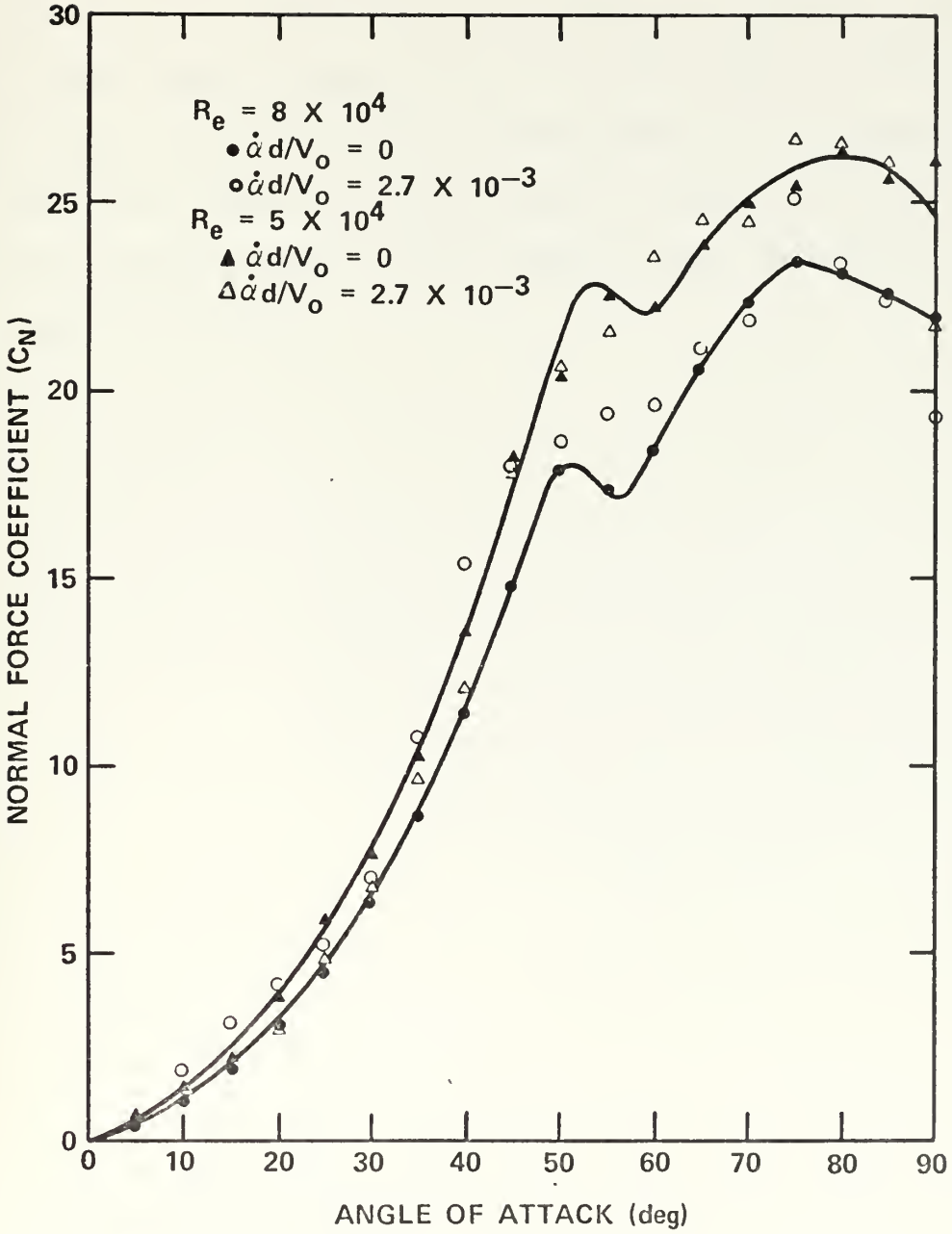

Figure 26. Normal force coefficient variation with angle of attack for various Reynolds numbers at a constant value of the pitch rate parameter

in the normal force for low angles of attack where the axial flow dominates. In other words, even though the freestream Reynolds number is constant, the local crossflow Reynolds number is affected by the rate of pitch. This description seems to be valid only if the freestream Reynolds number is such that the increment of velocity due to pitch causes some change in the flow state, at a station where the local flow conditions control a large portion of the flowfield about the remainder of the body.

CONCLUSIONS

The results of this experimental investigation serve to establish baseline static aerodynamic data for a particular configuration and to illustrate the influence of a constant rate of pitch upon the aerodynamic loads for large excursions in angle of attack. In addition, flow transitions within the wake vortex system were observed during the flow visualization studies and correlated with observed changes in the force and moment coefficients. The results presented herein, although not directly applicable to the design of a missile airframe, do provide additional insight into some of the potential flow anomolies that may occur during an actual flight or during wind tunnel tests.

The results of this investigation show that there is an increment of normal force directly attributable to the uniform pitching motion. While undergoing uniform pitching, the normal force curve has a steeper slope (C_{N_α}), reaches the inflection point at a slightly higher angle of attack and the inflection is less abrupt. The increment of normal force due to uniform pitching is closely coupled to the Reynolds number, and may only be apparent if the angular velocity induces a local velocity increment at a station where the crossflow Reynolds number would otherwise remain at a threshold to some change in the separation angle, boundary layer transition point, or change in the wake vortex configuration. The increment of normal force due to uniform pitching has implications for the calculation of stability derivatives (C_{N_α}) for motions involving large excursions in angle of attack.

It was observed that for pitch rates of less than 20 degrees per second the normal force curve is not significantly different from the static case, at least up to about 50 degrees angle of attack. Beyond 50 degrees the difference may be sufficient to indicate some consistent pitch rate dependence. It must be cautioned that these results were obtained while pitching the body about a point which nearly coincides with the center of the frontal area. The identification of a maximum pitch rate at which a body can be rotated, such that the normal force is still essentially that for the static case, must include a definition of where the axis of rotation is located. That is, it appears possible to rotate a body about an axis such that the increment of normal force due to a constant angular velocity could be nullified.

These results have significant implications for experimentors conducting wind tunnel tests where the model is rapidly rotated in order to obtain "static" data for large variations in the angle of attack during a short period of time. Rapidly sweeping the model is a common occurrence when using blowdown type wind tunnels. Also, quite often these models are rotated about an axis well aft of the base of the model, only serving to exaggerate the effect of the angular velocity.

Although an increment of normal force was observed during these experiments, the potential magnitude of the effects of pitch rate were not fully investigated. It is suggested that additional experiments be conducted to verify the significance of the location of the axis of rotation. In addition, alternate nose geometries should be investigated since the persistence of the axial flow component even at the very high angles of attack may cause more significant pitch rate effects depending upon the development of the crossflow along the axis.

APPENDIX A

FLOW VISUALIZATION STUDIES

The extent to which measured aerodynamic loads can be expected to fully illustrate the causes of particular phenomena is limited due to the integrated nature of balance derived aerodynamic forces. For the case of an inclined axisymmetric body the loads are developed primarily as a consequence of a complex wake flow system. The wake vortex pattern is known to undergo a number of transitions with increasing angle of attack; however, the identification of the local angle of attack, and the axial station along the body at which these transitions occur, are not always obvious from the integrated force and moment coefficient data.

In order to correlate specific irregularities in the force and moment coefficient curves with wake flow transitions, a smoke flow visualization technique was employed. The smoke generator was similar to the one described by Yu, Sparrow and Eckert [Ref. 19]. The smoke was injected using a multi-tube rake placed upstream of the wind tunnel inlet and turbulence control screens. It was not necessary to disturb any of the test apparatus in order to conduct these studies. It was found that photographic quality smoke could be generated for approximately fifteen minutes while operating the wind tunnel at a nominal speed of 70 feet per second. The model was illuminated with two 600 watt photo-flood lamps shining through a slit in the test section floor. The model was pitched down instead of up in order to eliminate the shadow of the sting in the wake region. Both still and

motion picture photography was used to record the wake flow patterns made visible by the smoke.

The motion picture (16mm colored film) was edited to approximately twelve minutes of run time. The film was divided into three segments; (1) a sequence at fixed angles of attack, (2) a segment showing continuous sweeps in pitch and (3) a series at specific angles of attack to illustrate the unstable nature of the wake. Some of the more important features of the wake vortex flow patterns illustrated in the film include:

(1) At low angles of attack the axial flow component dominates the wake flow pattern.

(2) For angles of attack below about 20 degrees the wake is essentially a pair of rolled-up vortex sheets (NACA vortex model) extending the entire length of the body.

(3) For angles of attack between 20 and 50 degrees the wake vortex pattern is that of steady asymmetric shedding of discrete trailing vortices. The number of discrete vortices trailing from a body of a given length increases with increasing angle of attack.

(4) At an angle of attack of about 60 degrees the flow on the afterbody is dominated by the crossflow component while the axial flow still controls the wake on the nose section. Between 60 and 70 degrees this axial flow component persists but becomes very unstable on the nose section.

(5) Above angles of attack of 70 degrees the wake flow is dominated by the crossflow component except very near the apex of the nose.

(6) During a continuous sweep in pitch (approximately five degrees per second) the wake flow appears to undergo smooth transitions in its basic character except at about 60 degrees, where a temporary instability is often characteristic.

Figures 27 through 39 are a series of still photographs. In all cases the model was pitched down and the camera was located slightly below and downstream of the axis of rotation. Figures 27 through 29 are illustrations of the axially dominated steady asymmetric shedding of discrete vortices. At an angle of attack of 38 degrees a second vortex trail is just forming at the base of the model. With increasing angle of attack the second vortex detaches at an axial station further forward from the base. At an angle of attack of 55 degrees (Figure 30) the flow on the afterbody is undergoing a transition from a flow dominated by the axial component to a flow dominated by the crossflow. However, a distinct vortex continues to emanate from the nose section.

While increasing the angle of attack from 55 degrees to 68 degrees (Figures 31 through 34) the crossflow becomes more and more predominant until, at 68 degrees, the axial flow component is almost nonexistent. The axial flow influence on the nose vortex was very intermittent in this angle of attack range, thus making it difficult to capture the true character of this instability in still photographs. At 70 degrees (Figure 35) the wake is almost entirely dominated by the crossflow component and more of the near wake becomes turbulent. At both 70 and 75 degrees (Figure 35 and Figure 36) a slight axial flow influence still remains near the apex of the nose. Figures 37 through 39 were included for completeness, showing a turbulent wake

Figure 27. Still photograph of the model at an angle of attack of 38 degrees

Figure 28. Still photograph of the model at an angle of attack of 43 degrees

Figure 29. Still photograph of the model at an angle of attack of 50 degrees

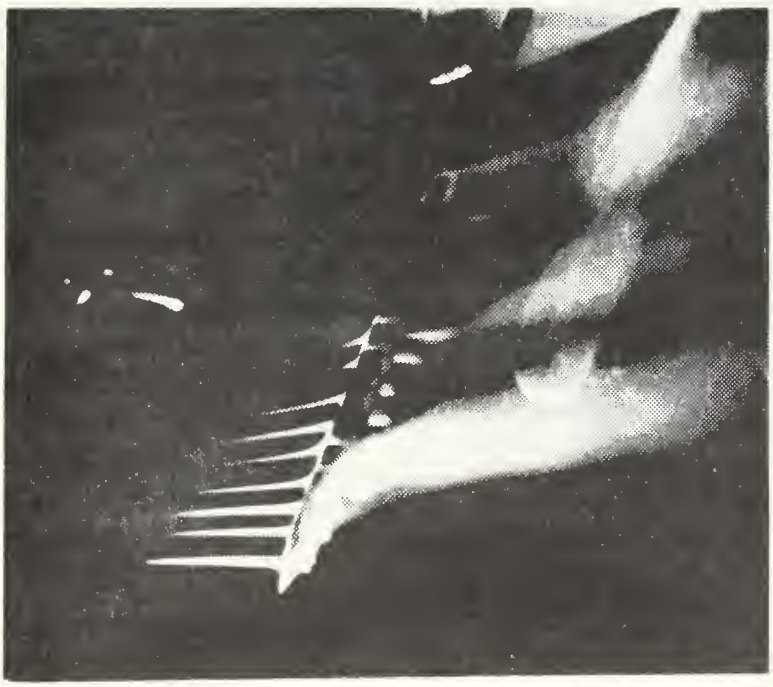

Figure 30. Still photograph of the model at an angle of attack of 55 degrees

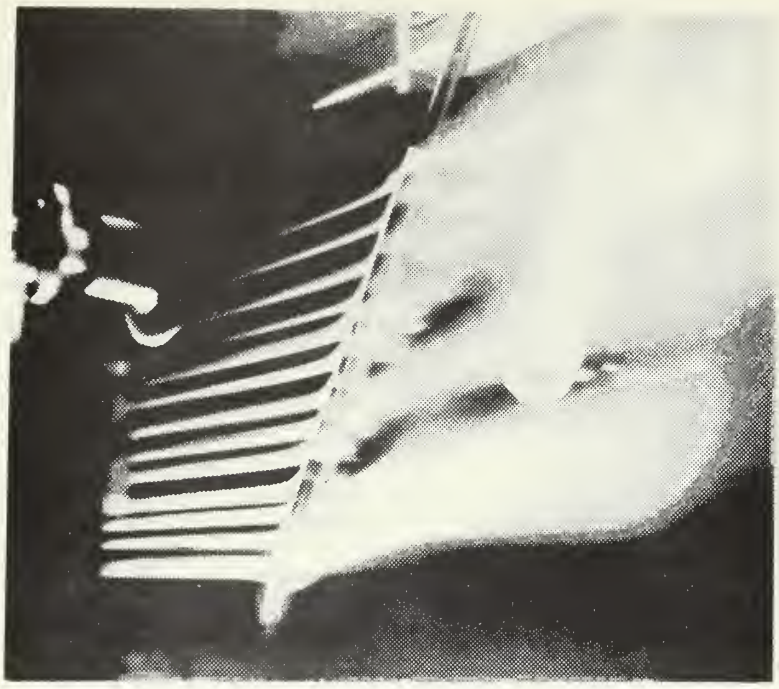

Figure 31. Still photograph of the model at an angle of attack of 60 degrees

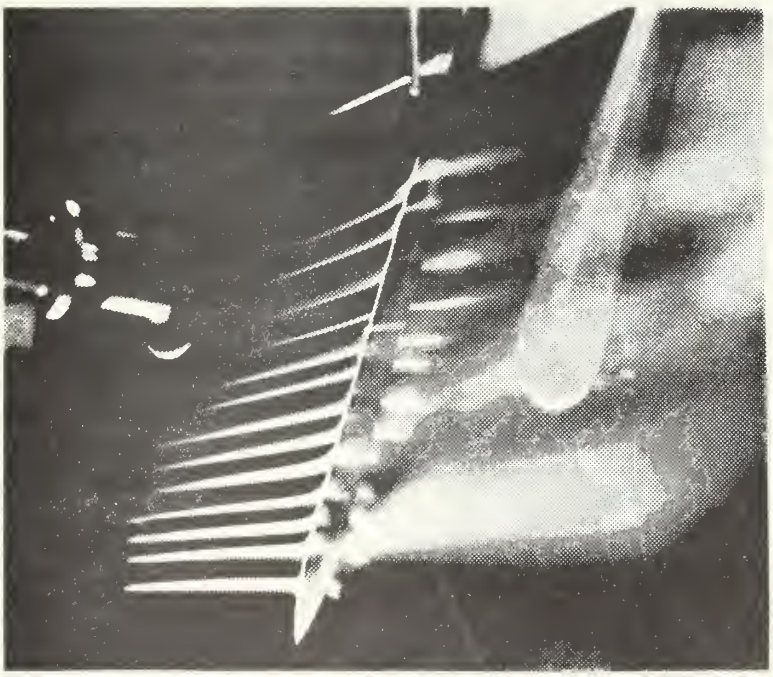

Figure 32. Still photograph of the model at an angle of attack of 63 degrees

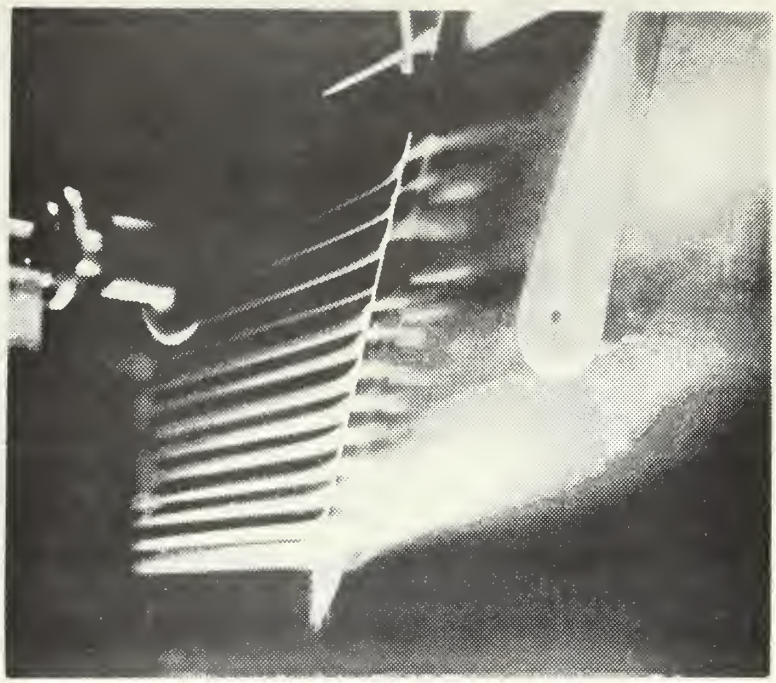

Figure 33. Still photograph of the model at an angle of attack of 65 degrees

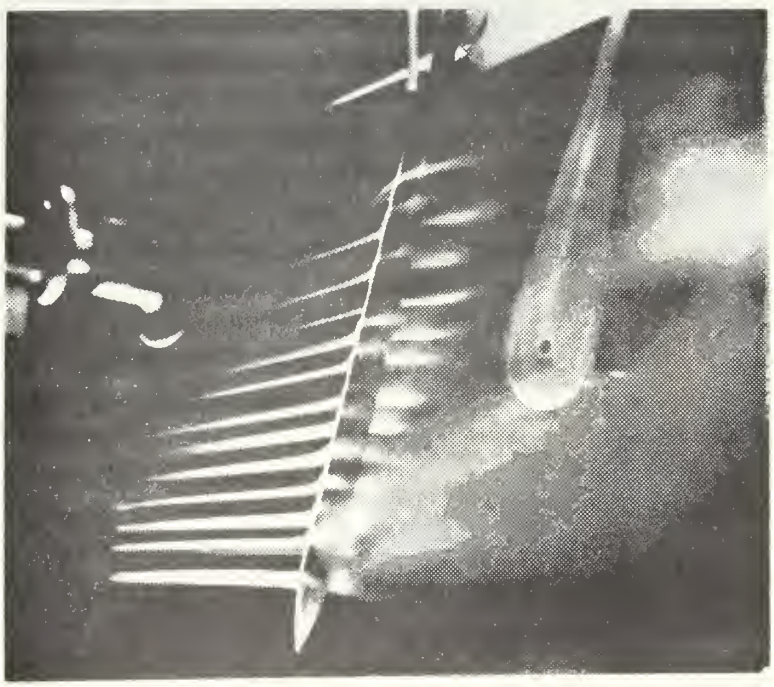

Figure 34. Still photograph of the model at an angle of attack of 68 degrees

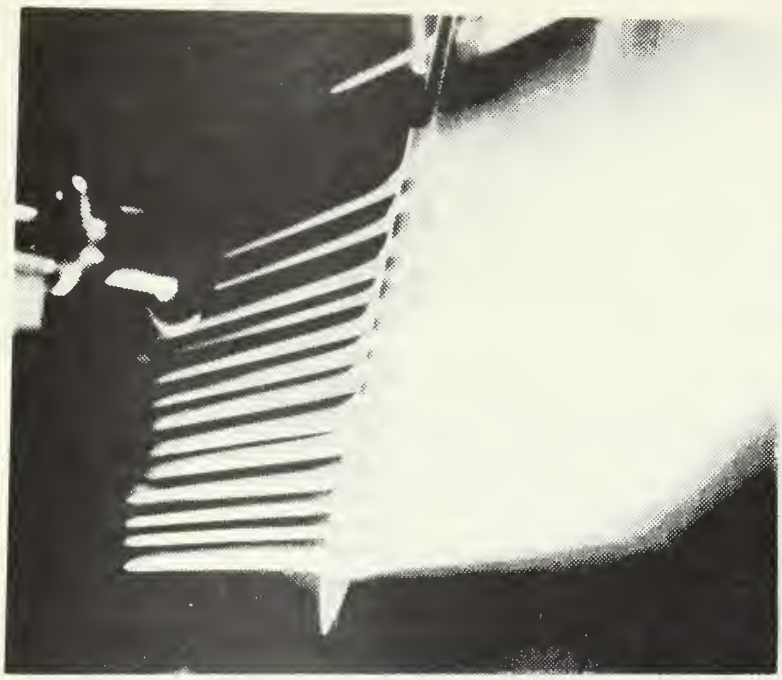

Figure 35. Still photograph of the model at an angle of attack of 70 degrees

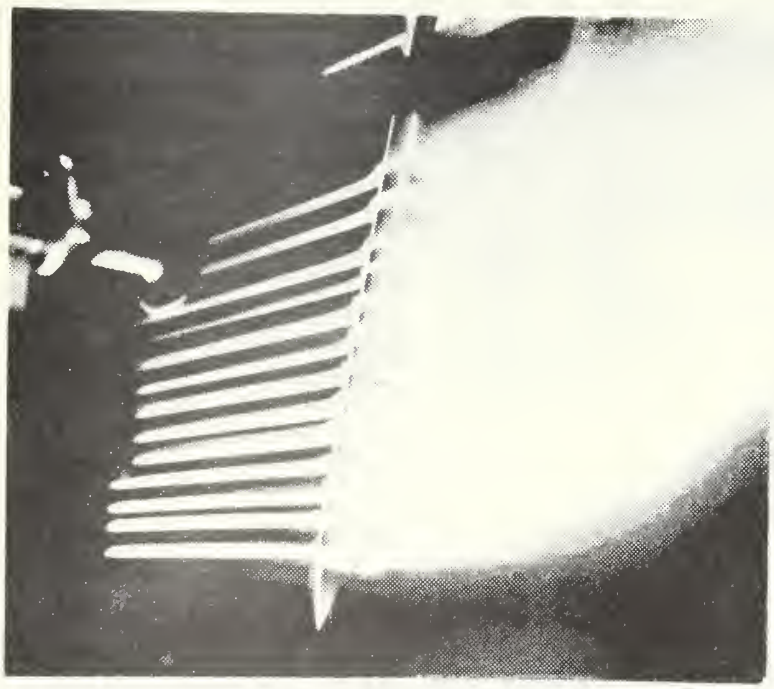

Figure 36. Still photograph of the model at an angle of attack of 75 degrees

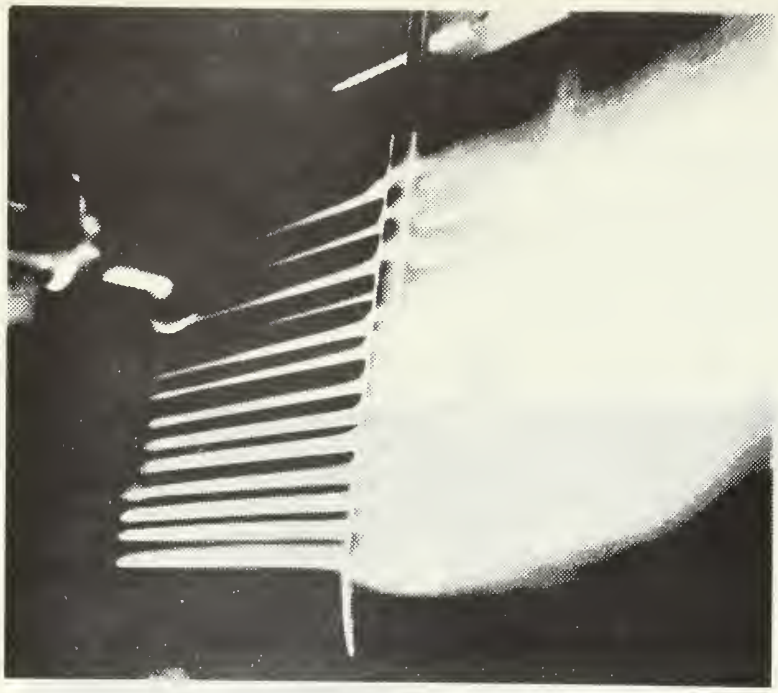

Figure 37. Still photograph of the model at an angle of attack of 80 degrees

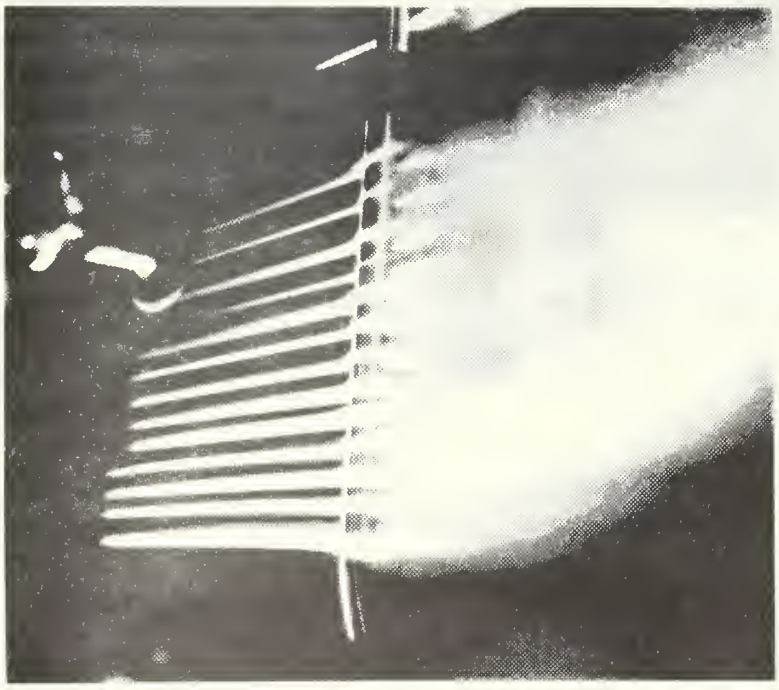

Figure 38. Still photograph of the model at an angle of attack of 85 degrees

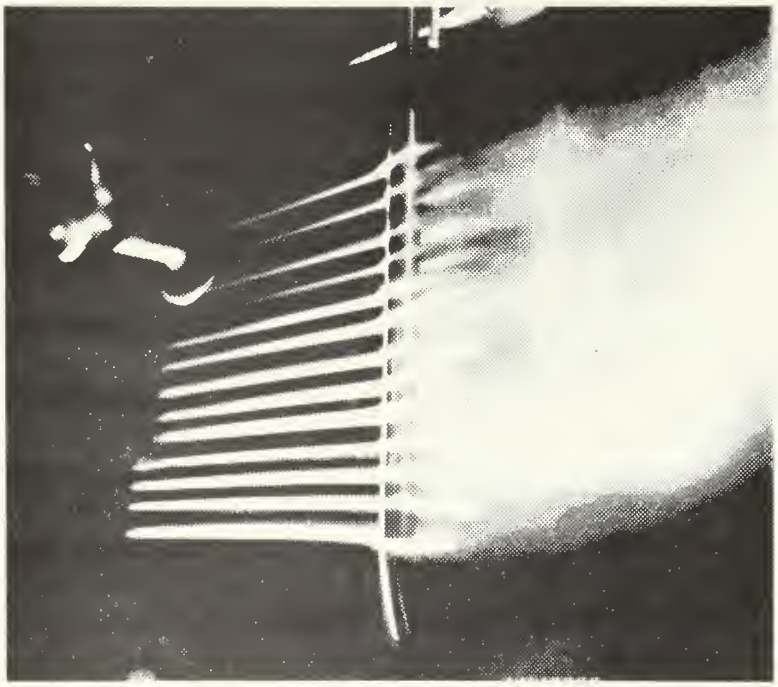

Figure 39. Still photograph of the model at an angle of attack of 90 degrees

entirely dominated by the crossflow component of the freestream velocity.

This sequence of photographs shows how the system of trailing vortices dominated by an axial flow component undergoes the transition to a wake dominated by the crossflow component. Flow instabilities often occur during this transition with the last remaining vortex near the apex of the nose alternating between a trailing vortex (axial component) and a separated crossflow behind a nearly normal cylinder.

APPENDIX B

BALANCE INTERACTIONS STUDY

Internal balances are rarely entirely free of interactions of one component of load on the measurement of other components. Balance interactions are reduced to equation form and generally include both first and second order terms. To illustrate, consider the normal force interaction equation

$$N = N' - \left[N'(N/N) + S'(N/S) + A'(N/A) + m'(N/m) + n'(N/n) + R'(N/R) + (N')^2(N/N^2) + (S')^2(N/S^2) + (A')^2(N/A^2) + (m')^2(N/m^2) + (n')^2(N/n^2) + (R')^2(N/R^2)\right]$$

where the primes denote actual readings under the combined loads. Each of the coefficients in this equation were evaluated[5], and following the procedure outlined by Hausen [Ref. 20] the magnitude

---

[5] HB-2 balance calibration data, 18 January 1972, Naval Ship Research and Development Center, Carderock, Maryland.

of each term can be estimated in percent of the full scale deflections. The corrected normal force can be expressed as

$$\text{Normal force} = \frac{\text{Normal force reading}}{\text{Normal force sensitivity}} - \varepsilon_N$$

where

ε_N =	+0.00000 N'	0.0%[6]
	+0.00000 S'	0.0%
	+0.00422 A'	0.3%
	-0.01350 m'	4.0%
	+0.00269 n'	0.7%
	+0.00102 R'	0.2%
	+0.00063 $(N')^2$	1.6%
	+0.00000 $(S')^2$	0.0%
	+0.00011 $(A')^2$	0.1%
	+0.00013 $(m')^2$	3.0%
	-0.00006 $(n')^2$	0.9%
	-0.00006 $(R')^2$	0.4%

As suggested in Ref. 20, all interactions less than 0.3 percent may readily be eliminated as negligible. The remaining interaction terms may be required in certain tests, but it is frequently possible to eliminate many and sometimes all of the interaction terms on the basis of their being negligible under the test conditions expected.

---

[6] The load contribution on one component due to a positive design load applied to another component.

For example, in the present investigation there are no roll moments to be expected, thus any contribution due to R' and $(R')^2$ can be ignored. Since the maximum loads experienced in these experiments were considerably less than the design loads for the balance, neglecting all of the interaction terms for the normal force at the expected loads causes an error of less than one percent. This error is about half the total experimental uncertainty discussed in Appendix C. Therefore, it was concluded that neglecting all balance interactions during these experiments would not significantly alter the experimental results.

APPENDIX C

UNCERTAINTY AND ERROR ANALYSIS OF EXPERIMENTAL DATA

In using experimental data to establish fundamental trends one must always be attendant to experimental uncertainties. Ideally, measurements would be repeated enough times using different observers and techniques so that the reliability of the results could be assured by the use of statistics. Too often this is not possible.

For single or very small samples the observer's estimate of what the error might be is the uncertainty. Kline and McClintock [Ref. 21] presented a method for describing the way in which these uncertainties propogate in the analysis of experimental data. Following their approach, the aerodynamic coefficients were expressed in the following form:

$$C = F/kV^2$$

where it has been assumed that there were no uncertainties in the determination of the air density or the body reference diameter. The uncertainty in the coefficient is then given by

$$\omega_C = \left[\left(\frac{\partial C}{\partial F} \right)^2 \omega_F^2 + \left(\frac{\partial C}{\partial V} \right)^2 \omega_V^2 \right]^{1/2}$$

Upon substitution for the derivatives obtain

$$\left(\frac{\omega_C}{C} \right)^2 = \left(\frac{\omega_F}{F} \right)^2 + \left(-2 \frac{\omega_V}{V} \right)^2$$

The velocity, however, was not recorded directly but was calculated from the anemometer output voltage. The velocity and anemometer output voltage are related by

$$V = \left(\frac{E^2 - E_o^2}{\beta}\right)^2 = \frac{E^4 - 2E_o^2E^2 + E_o^4}{\beta^2}$$

Then, assuming the calibration constants E_o and β were determined without error, obtain

$$\left(\frac{\omega_V}{V}\right)^2 = \left[\frac{4}{1-(E_o/E)^2}\right]^2\left(\frac{\omega_E}{E}\right)^2$$

Inserting the above equation for the uncertainty in velocity into the equation for the uncertainty in the coefficient, obtain

$$\left(\frac{\omega_C}{C}\right)^2 = \left(\frac{\omega_F}{F}\right)^2 + \left[\frac{8}{1-(E_o/E)^2}\right]^2\left(\frac{\omega_E}{E}\right)^2$$

The experimental uncertainty in the aerodynamic coefficient has been expressed in terms of the uncertainty in the force or moment and the anemometer output voltage. The uncertainties in each of these measured parameters were determined by noting the precision with which they could be measured. It has been noted that the normal force could be interpreted to ± 0.02 pounds, while the anemometer output voltage could be resolved to ± 0.001 volt. Using these limits of resolution, the experimental uncertainty in the normal force coefficient was calculated for a typical example, the results of which are presented in Figure 40. The major contributor to this uncertainty in the coefficient, using the above limits of resolution, was the uncertainty in the measured load and not the anemometer output voltage. The uncertainty in the pitching moment coefficient would be identical to

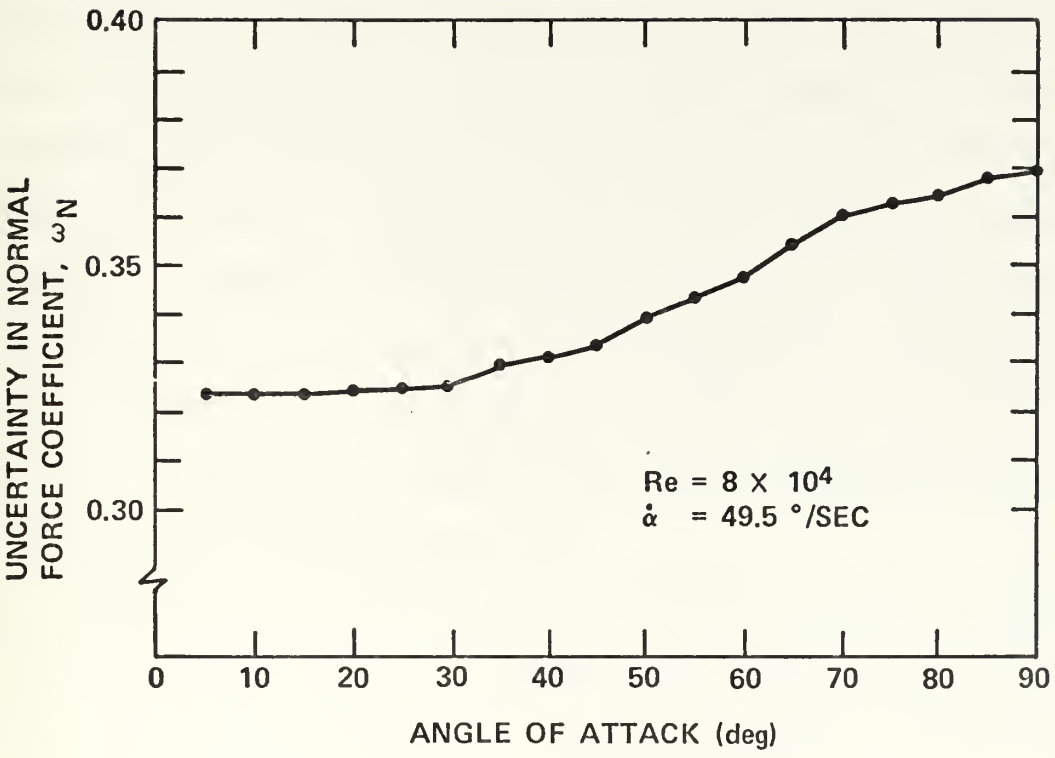

Figure 40. Uncertainty in the normal force coefficient due to the limits of resolution of the experimental data

that for the normal force coefficient since the reference diameter was assumed to be determined without error.

A limited number of the experiments were duplicated in order to test the reproducibility of the experimental data. Figure 41 shows data points for five separate runs at $R_e = 8X10^4$ and $\dot{\alpha} = 49.5$ degrees per second where the mean value has been drawn as a continuous curve. An estimate of the standard deviation of this relatively small sample was obtained by dividing the maximum spread in the data points by the square root of the number of points used in the sample. The percent deviation about the mean value is presented in Figure 42. For the same data the percent uncertainty was also calculated and is shown in Figure 42. Comparing the two curves in Figure 42 it is seen that the deviation about the mean value for identical runs was about the same as the uncertainty in the measurements. Therefore, further improvements in the experimental data could only be achieved through the use of instruments with greater resolution.

Referring again to Figure 40, note that the variation in uncertainty of the coefficient increases slightly over the angle of attack range. Thus, establishing a uniform uncertainty band of ± 0.4, the odds that any experimental data point will lie within these limits have been improved. It was concluded that the coefficients could be represented by single points or the mean values for multiple observations with an uncertainty of no more than ± 0.4 in the value of the coefficient throughout the angle of attack range with a relatively high degree of confidence. The identification of the uncertainty band provides the limits within which trends can be established.

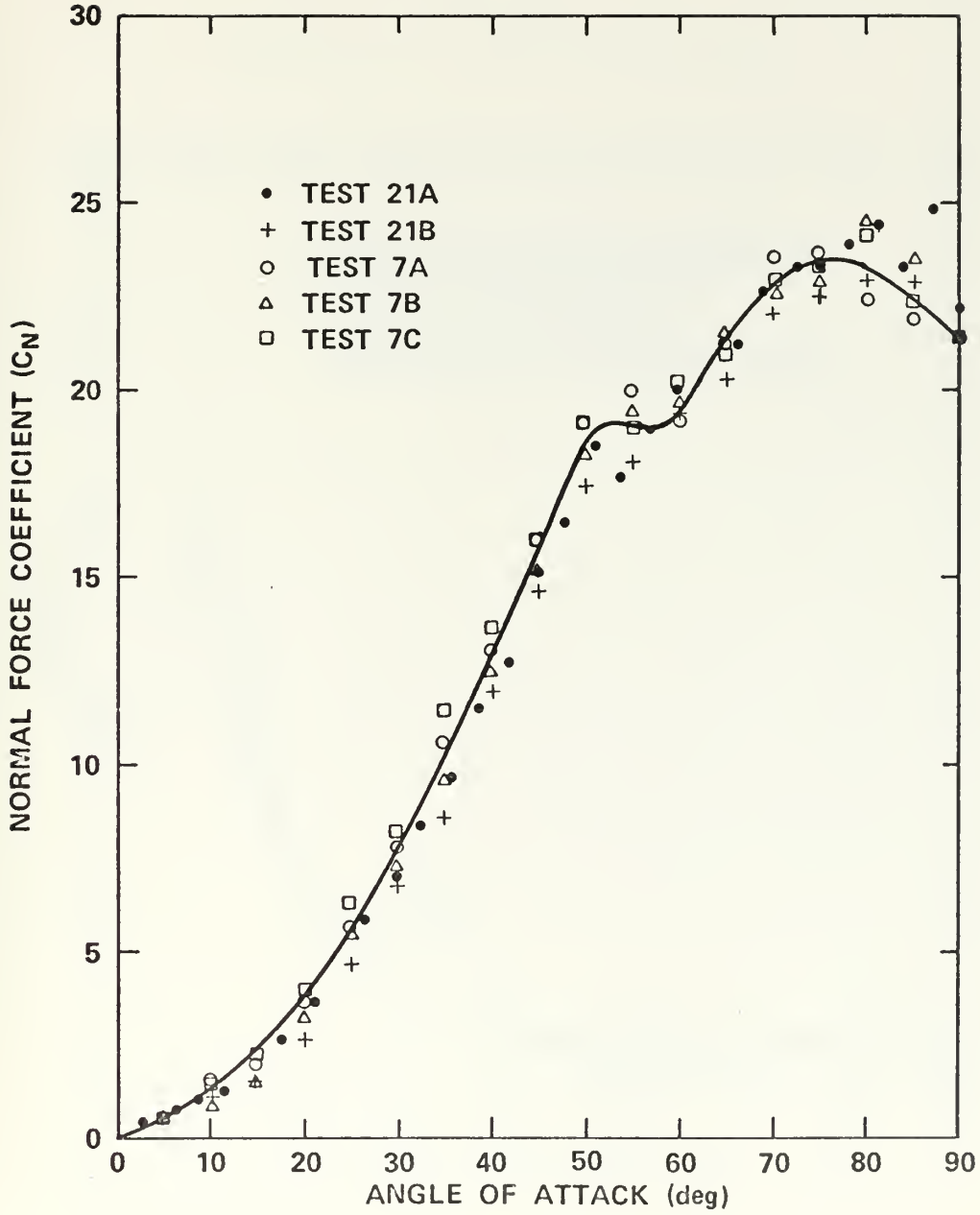

Figure 41. Reproducibility of the normal force coefficient for multiple tests

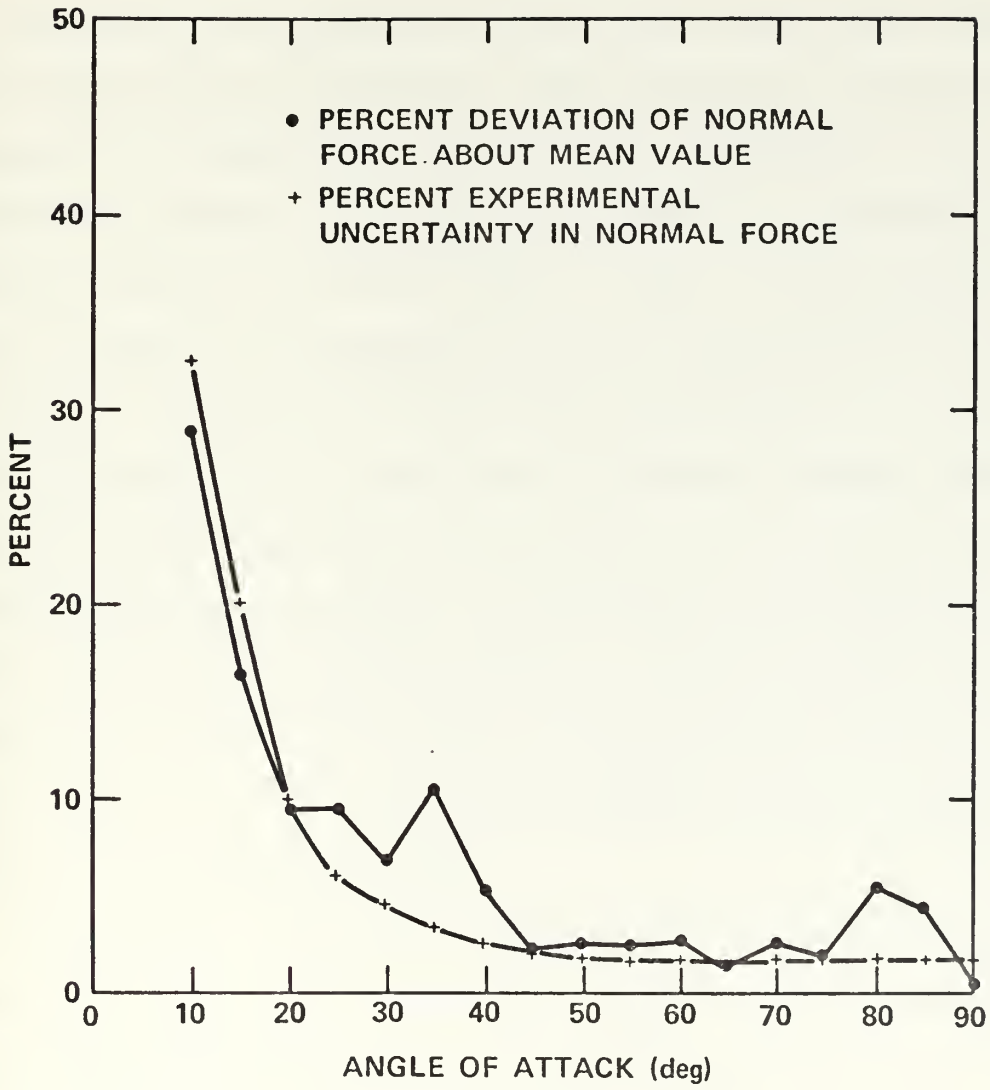

Figure 42. Comparison of random errors and uncertainty

APPENDIX D

COMPARISONS OF THE EXPERIMENTAL DATA

Body fineness has a definite effect on the normal force coefficient for inclined bodies of revolution, since increasing the fineness ratio increases the normal force through sectional contributions on the cylindrical afterbody. Increased body fineness also decreases the relative influence of the nose section. Figure 43 was developed in order to compare the experimental results of this study with the data of others. Although an effort was made to obtain data for a similar body, the referenced data used in this illustration includes results obtained with different fineness proportions, for both subcritical and supercritical Reynolds numbers, for compressible and incompressible flows, and for various mounting schemes. The ranges of these variables are listed in Table I. The effects of the mounting scheme cannot be truly assessed since it is not always clear how the models were supported in the referenced material.

The agreement of the present results with the referenced data for angles of attack up to 40 degrees is quite good. Above 40 degrees angle of attack the normal force becomes more sensitive to the length to diameter ratio since the end relieving effects are conveyed to other sections of the body. Also, as illustrated in Appendix A, an axial flow component can persist on the nose section even up to 90 degrees angle of attack. Thus, both body fineness and nose fineness

can significantly influence the pressure distribution along the body and the wide variation in the data at the higher angles is understandable.

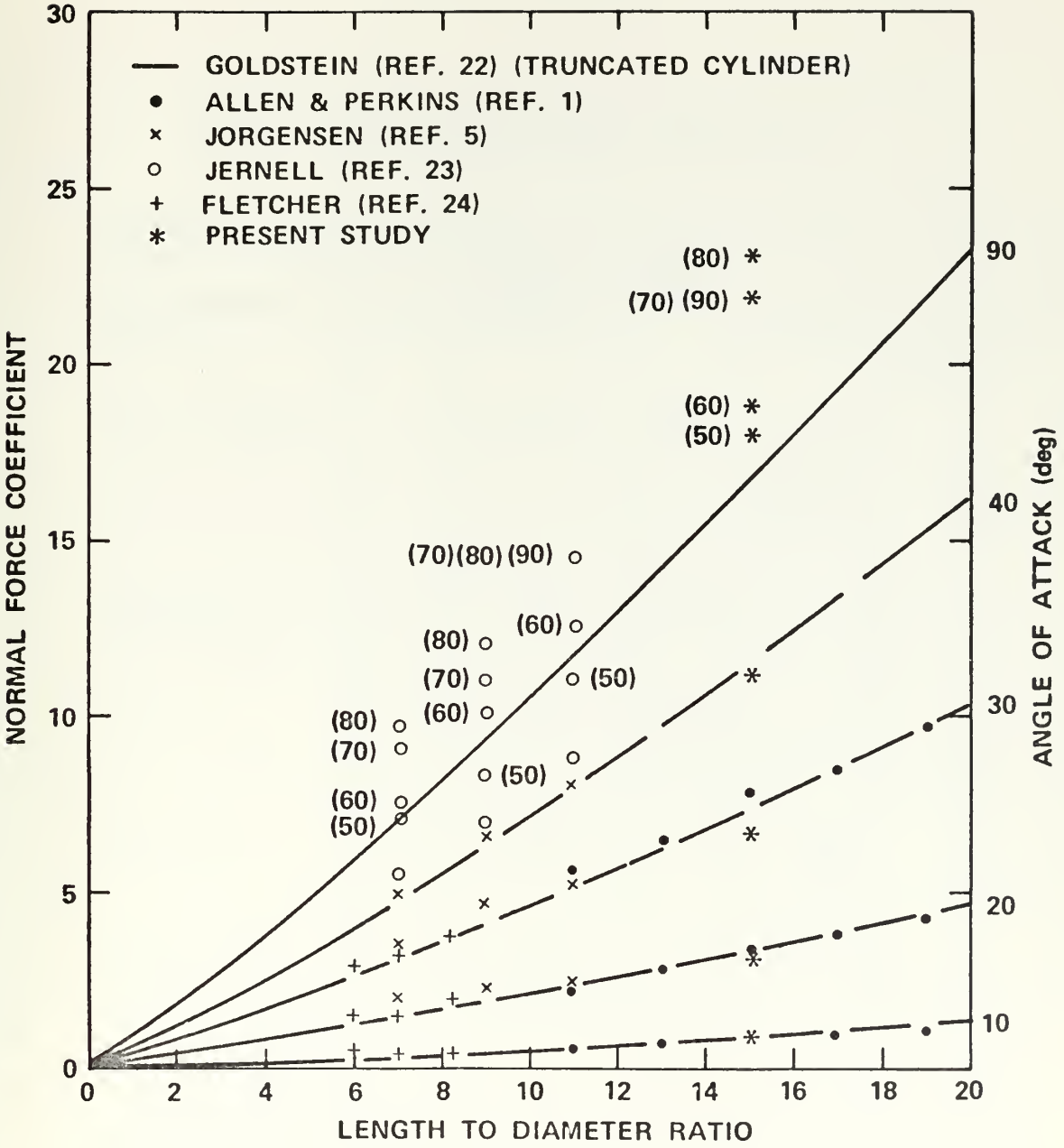

Figure 43. The effect of body fineness on the normal force for tangent ogive/cylinders

Table I. Flow parameters and body geometry for referenced data

Source of Data	Ref.	Reynolds Number	Mach Number	ℓ/d	ℓ_N/ℓ
Goldstein	22	$8.8X10^4$	--	variable	truncated cylinder
Allen & Perkins	1	$3.9X10^5$	1.98	11.1	.30
				13.1	.30
				15.1	.30
				17.1	.30
				19.1	.30
Jorgensen	5	10^5	2.86	7.	.71
				9.	.56
				11.	.45
Jernell	23	10^5	1.50	7.	.71
				9.	.56
				11.	.45
Fletcher	24	$5.0X10^4$	--	5.90	.26
				7.07	.21
				8.25	.18
Present study	--	$1.4X10^5$	--	15.00	.20

LIST OF REFERENCES

1. National Advisory Committee for Aeronautics, NACA RM A50L07, Characteristics of Flow Over Inclined Bodies of Revolution, by H. J. Allen and E. W. Perkins, 29 January 1951.

2. Naval Postgraduate School, NPS-59NN72082A, Flow Studies of Axisymmetric Bodies at Extreme Angles of Attack, by L. H. Smith and R. H. Nunn, 18 August 1972.

3. National Advisory Committee for Aeronautics, Report 1048, A Study of Effects of Viscosity on Flow Over Slender Inclined Bodies of Revolution, by H. J. Allen and E. W. Perkins, 1951.

4. Kelly, H. R., "The Estimation of Normal-Force, Drag, and Pitching-Moment Coefficients for Blunt-Based Bodies of Revolution at Large Angles of Attack," Journal of the Aeronautical Sciences, v. 21, no. 8, p. 549-565, August 1954.

5. National Aeronautics and Space Administration, NASA TN D 6996, Prediction of Static Aerodynamic Characteristics for Space-Shuttle-Like and Other Bodies at Angles of Attack From 0° to 90°, by L. H. Jorgensen, January 1973.

6. Weapons Research Establishment (Australia) Report 782, The Estimation of Viscous Normal Force, Pitching Moment, Side Force and Yawing Moment on Bodies of Revolution at Incidences Up to 90°, by K. D. Thomson, October 1972.

7. Bryson, A. E., "Symmetric Vortex Separation on Circular Cylinders and Cones," Journal of Applied Mechanics, v. 26, no. 4, p. 643-648, December 1959.

8. Sarpkaya, T., "Separated Flow About Lifting Bodies and Impulsive Flow About Cylinders," AIAA Journal, v. 4, no. 3, p. 414-420, March 1966.

9. Schindel, L. H., "Effects of Vortex Separation on the Lift Distribution on Bodies of Elliptic Cross Section," Journal of Aircraft, v. 6, no. 6, p. 537-543, November-December 1969.

10. Angelucci, S. B., "A Multivortex Method for Axisymmetric Bodies at Angle of Attack," Journal of Aircraft, v. 8, no. 12, p. 959-966, December 1971.

11. Naval Ordnance Laboratory Report 73-209, Prediction of Normal Force, Pitching Moment, and Yawing Forces on Bodies of Revolution at Angles of Attack Up to 50 Degrees Using a Concentrated Vortex Flow-Field Model, by A. B. Wardlaw, 24 October 1973.

12. Sarpkaya, T., "Separated Unsteady Flow About a Rotating Plate," Developments in Mechanics, v. 4, p. 1485-1499, 1968.

13. Aeronautical Research Council (Great Britian) Reports and Memorandum No. 1216, The Lift and Pitching Moment on an Aerofoil Due to a Uniform Angular Velocity of Pitch, by H. Glauert, p. 636-646, November 1928.

14. Schlichting, H., Boundary Layer Theory, 4th ed., p. 27-32, 146-155 and 252, McGraw Hill, 1960.

15. Goldstein, S., editor, Modern Developments in Fluid Dynamics, v. I, p. 65, Oxford Press, London, 1938.

16. Naval Ship Research and Development Center Report 3647, Location of Separation on a Circular Cylinder in Crossflow as a Function of Reynolds Number, by D. W. Coder, November 1971.

17. Naval Ordnance Test Station NAVORD Report 3529 (NOTS 1166), The Subsonic Aerodynamic Characteristics of Spinning Cone-Cylinders and Ogive-Cylinders at Large Angles of Attack, by H. J. Hauer and H. R. Kelly, 11 July 1955.

18. Thomson, K. D. and Morrison, D. F., "The Spacing, Position and Strength of Vortices in the Wake of Slender Bodies at Large Incidence," Journal of Fluid Mechanics, v. 50, part 4, p. 751-783, December 1971.

19. Yu, J. P., Sparrow, E. M., and Eckert, E. R. G., "A Smoke Generator for Use in Fluid Flow Visualization," International Journal of Heat and Mass Transfer, v. 15, p. 557-558, 1972.

20. Advisory Group for Aeronautical Research and Development AGARD Report 13, Evaluation and Calibration of Wire-Strain-Gage Wind Tunnel Balances Under Load, by R. M. Hausen, February 1956.

21. Kline, S. J. and McClintock, "Describing Uncertainties in Single-Sample Experiments," Mechanical Engineering, p. 3-8, January 1953.

22. Goldstein, S., editor, Modern Developments in Fluid Dynamics, v. II, p. 439, Oxford Press, London, 1938.

23. National Aeronautics and Space Administration, NASA TM-X-1658, Aerodynamic Characteristics of Bodies of Revolution at Mach Numbers from 1.50 to 2.86 and Angles of Attack to 180°, by L. ". Jernell, October 1968.

24. Weapons Research Establishment (Australia) Report HSA 159, Investigation of the Magnus Characteristics of a Spinning Inclined Ogive-Cylinder Body at M = 0.2, by C. A. J. Fletcher, October 1969.

INITIAL DISTRIBUTION

	No. Copies
Defense Documentation Center Cameron Station Alexandria, Virginia 22134	2
Naval Postgraduate School Monterey, California 93940	
Department of Mechanical Engineering	
Assoc. Prof. R. H. Nunn	1
Prof. T. Sarpkaya	1
Prof. G. Cantin	1
Assoc. Prof. T. M. Houlihan	1
Department of Mathematics	
Prof. G. W. Morris	1
Department of Aeronautics	
Assoc. Prof. D. W. Netzer	1
Library	2
Naval Weapons Center China Lake, California 93555	
Code 533 (Technical Library)	1
Code 512	1
Code 3124 (Dr. W. Clark)	1
Code 45	1
Code 45602 (L. H. Smith)	1